CrossMark

ORIGINAL ARTICLE

Synergy temporal sequences and topography in the spinal cord: evidence for a traveling wave in frog locomotion

Philippe Saltiel[1] · Andrea d'Avella[1,2,3] · Kuno Wyler-Duda[1] · Emilio Bizzi[1]

Abstract Locomotion is produced by a central pattern generator. Its spinal cord organization is generally considered to be distributed, with more rhythmogenic rostral lumbar segments. While this produces a rostrocaudally traveling wave in undulating species, this is not thought to occur in limbed vertebrates, with the exception of the interneuronal traveling wave demonstrated in fictive cat scratching (Cuellar et al. J Neurosci 29:798–810, 2009). Here, we reexamine this hypothesis in the frog, using the seven muscle synergies A to G previously identified with intraspinal NMDA (Saltiel et al. J Neurophysiol 85:605–619, 2001). We find that locomotion consists of a sequence of synergy activations (A–B–G–A–F–E–G). The same sequence is observed when focal NMDA iontophoresis in the spinal cord elicits a caudal extension-lateral force-flexion cycle (flexion onset without the C synergy). Examining the early NMDA-evoked motor output at 110 sites reveals a rostrocaudal topographic organization of synergy encoding by the lumbar cord. Each synergy is preferentially activated from distinct regions, which may be multiple, and partially overlap between different synergies. Comparing the sequence of synergy activation in locomotion with their spinal cord topography suggests that the locomotor output is achieved by a rostrocaudally traveling wave of activation in the swing–stance cycle. A two-layer circuitry model, based on this topography and a traveling wave reproduces this output and explores its possible modifications under different afferent inputs. Our results and simulations suggest that a rostrocaudally traveling wave of excitation takes advantage of the topography of interneuronal regions encoding synergies, to activate them in the proper sequence for locomotion.

Keywords Central pattern generator · Locomotion · Traveling wave · Synergy sequence · Synergy topography · Spinal cord

Introduction

Spinal cord central pattern generators (CPGs) are important, because they represent circuitry already capable to achieve a sophisticated motor output, independently of supraspinal and afferent inputs, and closely similar to that of the intact behaviors. There are different views about how spinal CPGs are organized. One view emphasizes a distributed representation which is not focal, except for a rostrocaudal gradient of excitability (Deliagina et al. 1983; Kjaerulff and Kiehn 1996). Another view suggests that specific segments of the lumbar cord, either rostral (Cazalets et al. 1995) or mid-segments (Marcoux and Rossignol 2000), are crucial to the function of the CPG. A recent optogenetic study supports a focal organization whereby different regions of the spinal cord might independently be responsible for different components of the motor pattern, defined as activations of individual muscles (Hägglund et al. 2013). This is similar to the concept of unit burst generators (Grillner 1981). Other studies (Patla 1985; Davis and Vaughan 1993; Olree and Vaughan 1995;

✉ Philippe Saltiel
  saltiel@mit.edu

1 Department of Brain and Cognitive Sciences, McGovern Institute for Brain Research, Massachusetts Institute of Technology, 77 Massachusetts Ave. 46-6189, Cambridge, MA 02139, USA

2 Department of Biomedical Sciences and Morphological and Functional Images, University of Messina, Messina, Italy

3 Laboratory of Neuromotor Physiology, Santa Lucia Foundation, Rome, Italy

Springer

Ivanenko et al. 2004) have emphasized temporal components, where independently of the exact muscle pattern, groups of muscles are activated at specific times. For example, locomotor temporal components are conserved phylogenetically, and partly from the newborn to the adult (Dominici et al. 2011). These two views of specific muscle activations, and of specific times of activation are to some extent represented in models which have suggested a two-layer organization for CPGs: a rhythm generation and a pattern formation layer (Lennard 1985; Burke et al. 2001; Saltiel and Rossignol 2004a, b; Rybak et al. 2006). Finally there is controversy as to whether a traveling wave of activation may be an important operating feature of CPGs (Cuellar et al. 2009; Pérez et al. 2009; AuYong et al. 2011).

With respect to activations of specific groups of muscles, synergies have been proposed as building blocks of motor control (Grillner 1981; Tresch et al. 1999; Ting and Macpherson 2004; Cheung et al. 2005, 2009; d'Avella et al. 2006; Krouchev et al. 2006; Yakovenko et al. 2011; Overduin et al. 2012; Berger et al. 2013; Bizzi and Cheung 2013; Krouchev and Drew 2013). There is also evidence that encoding of muscle synergies already takes place in the spinal cord (Saltiel et al. 2001; Stein 2008; Hart and Giszter 2010; Roh et al. 2011). In this paper, we are interested in whether the synergies are activated in specific sequences to construct movement. We also want to determine the synergy topography within the spinal cord, i.e., where the interneuronal regions encoding the different synergies are located. Comparing synergy sequences and topography should provide insight into how the spinal cord circuitry is laid out to produce synergy sequences and movement.

With focal intraspinal NMDA iontophoresis, we are able to obtain at 30 % of sites, generally rhythmic motor outputs with recording of isometric forces and EMGs from which we have extracted seven muscle synergies (Fig. 1b reproduced from Saltiel et al. 2001). Linear combinations of these synergies reconstruct the output with a mean R^2 of 91 %. Being interested in synergy sequences, we focus here on rhythms where the extension phase consists of a caudal extension-lateral force sequence. Caudal extensions and lateral forces primarily rely on hip and knee extensors, respectively. This sequence of forces is a priori a good starting point to study locomotion, since hip extensors finish earlier than knee extensors in the cat hind limb stance (Krouchev et al. 2006), and shoulder retractors and elbow extensors, respectively, dominate in early and late stance of cat forelimb fictive locomotion (Saltiel and Rossignol 2004a). With NMDA, the caudal extension-lateral force sequence is particularly seen when the caudal extension is of the type based on synergy B, which is linked to flexions starting with synergy F (Saltiel et al. 2005). We will focus

on this specific NMDA-evoked rhythm producing a caudal extension-lateral force-flexion cycle to identify the underlying synergy sequence. We will then study the synergy sequence in frog locomotion, and compare the two.

Because the site of application of NMDA is known each time, we will use the information obtained from all sites where NMDA evoked an output to learn about the synergy topography in the spinal cord.

Within the context of a two-layer CPG model, comparing the locomotor synergy sequence with synergy topography should provide insight into the pattern formation layer organization and connectivity in space. But it may also help to understand how the temporal organization of the synergies comes about, and therefore something about the layer organizing the temporal structure of the step cycle.
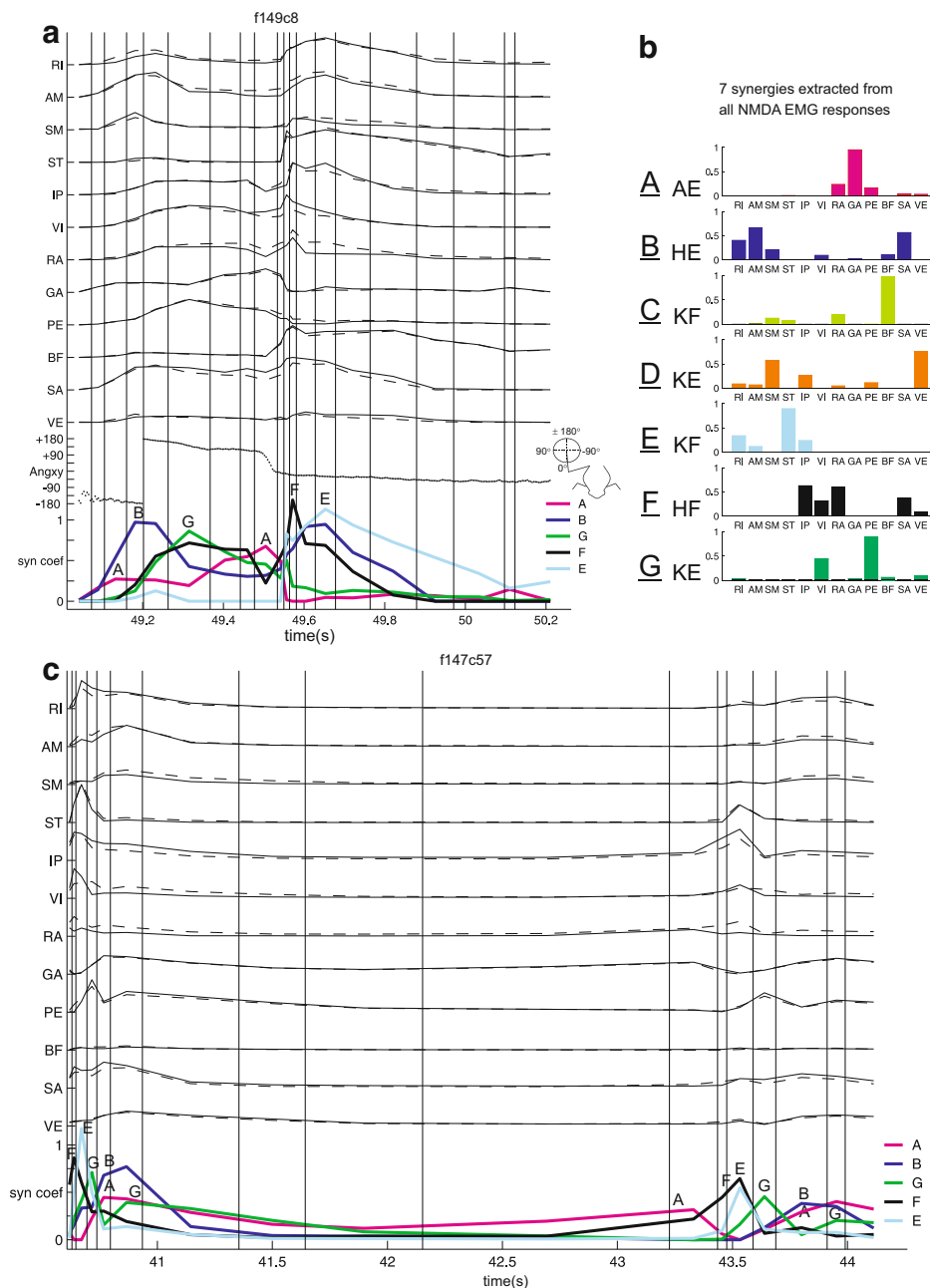
Our results from comparing synergy sequences and topography suggest that the hypothesis of a traveling wave of interneuronal activation in locomotion remains plausible. Thus, there would be evolutionary conservation in the adult frog of the traveling wave seen in tadpoles. We also present simulations reproducing the observed synergy sequence, and explore its modifiability by afferent input.

Results

Reconstruction of EMGs with synergies

Figure 1a shows an example of a caudal extension-lateral force-flexion sequence evoked by NMDA. The EMGs have been reconstructed with the seven synergies shown in Fig. 1b, and the coefficients of activation of synergies A, B, G, F, E are shown as colored lines. The agreement between observed (solid) and reconstructed (dashed) EMGs is generally good ($R^2 = 0.85$). Among the extensor synergies, A and B begin during the caudal extension phase, and G during the transition to the lateral force phase, followed by a second peak of synergy A activation. Flexion begins with a peak in synergy F, followed by E. Figure 1c is another example of a generally similar synergy sequence. Although no force was recorded (limb free), the initially flexor EMGs are produced by an F–E sequence, this time followed by a first synergy G activation peak in late flexion. This is followed by a prolonged extension phase which, similarly to Fig. 1a, begins with synergies A and B, followed by synergy G and finally by another synergy A peak. The sequence of synergies is seen to repeat over the beginning of the next cycle. Taken together, these two examples suggest an A+B–G–A–F–E–G synergy sequence in the extension–flexion cycle.

Reconstruction of NMDA-evoked EMGs with synergies. The A+B-G-A-F-E-G synergy sequence

Fig. 1 Reconstruction of EMGs of NMDA-evoked caudal extension-lateral force-flexion cycle, and the A+B–G–A–F–E–G synergy sequence. **a** Observed and reconstructed EMG responses are shown as *solid* and *dashed lines*, respectively. These *lines* join the average rectified EMG value at the mid-time of each manually parsed response, delimited by *vertical lines*. *RI* rectus internus, *AM* adductor magnus, *SM* semimembranosus, *ST* semitendinosus. *IP* iliopsoas, *VI* vastus internus, *RA* rectus anterior, *GA* gastrocnemius, *PE* peroneus, BF, biceps femoris, *SA* sartorius, *VE* vastus externus. Force angle trace below EMGs is oriented as shown in frog inset. The EMGs are reconstructed with the synergies A–G of Fig. 1b, and the coefficients of activation of synergies A, B, G, F and E for this reconstruction are shown as colored lines. The synergy sequence A–B–G–A–F–E is observed. The R^2 for the reconstruction was 0.85. Abscissa is in seconds after onset of NMDA iontophoresis (stopped at 30 s). This

site was located rostrocaudally at 85 % of 7–8th segment, 775 μm dorsoventral depth. **b** The seven synergies extracted from all NMDA EMG responses, labeled A–G (reproduced from Saltiel et al. 2001). The main actions of these synergies are indicated here and in subsequent figures: *AE* ankle extensor, *HE* hip extensor, *KF* knee flexor, *KE* knee extensor, *HF* hip flexor. Although synergy D also has HE function, in this paper where SM is activated less than VE, it is indicated as KE. **c** Another example of a similar synergy sequence, the illustration here beginning with flexion and F–E. There is now an intercalated G between the F–E and A+B–G–A of the subsequent prolonged extension, but otherwise the sequence is the same as in the example in **a**. The synergy sequence repeats itself over the beginning of the next cycle. The limb here was free (no force recorded). The R^2 for this reconstruction was 0.71. Abscissa is as in **a**. This site was located at 48 % of 9–10th segment and 850 μm depth

NMDA-evoked synergy sequence A–B–G–A–F–E–G

We now determine quantitatively the timing of synergy activations in the cycle, using the method illustrated in Fig. 2a (extension and flexion phase each divided in five equal bins). With each synergy given a value of 100 % at its maximum in the cycle, boxes represent the periods where their activations are above 70 %. Box height in each bin is determined by the relative order from most to least-activated synergies above the 70 % threshold. The A–B–G–A–F–E–G sequence is again seen.

Figure 2b plots the weighted centers of these boxes for 15 caudal extension-lateral force-flexion cycles evoked by NMDA at ten sites from six frogs. We generally see an A+B–G–A–F–E–G sequence. Figure 3a illustrates as angular histograms the distribution of the synergy activations shown in Fig. 2b. Each synergy clearly has preferred periods of activation in the cycle; the mean timing of these periods is shown as arrows. These arrows are reproduced in the lower right histogram, their amplitudes representing the number of observations averaged. The differences in orientation between consecutive arrows labeled A, B, G, A, F, E, G were all statistically significant ($P < .05$), except between F and E where it almost reached significance ($P = .0528$, unpaired t test, df 25) (Table 1). The results support the conclusion that the A–B–G–A–F–E–G synergy sequence characterizes the NMDA-evoked caudal extension-lateral force-flexion cycle.

Locomotor cycle synergy sequence A–B–G–A–F–E+G

We studied alternating terrestrial quadrupedal locomotion in the intact frog. Locomotion of the freely moving frog was sometimes spontaneous, but more often triggered by various manipulations: releasing the frog on the ground; sweeping a wet towel backwards from underneath the rear-body and hind limbs; cutaneous stimulation of various body parts with a fine forceps; passive hind limb extension.

Figure 2c illustrates an example of a step cycle (stance and swing each divided in five equal bins), with the EMGs reconstructed with the seven NMDA synergies. The agreement between observed (solid) and reconstructed (dashed) EMGs was fairly good ($R^2 = 0.70$ for 173 step cycles, and 0.76 in that example). The synergy activations, each plotted to a maximum of 100 % in the cycle, suggest an A–B–G–A–F–E+G sequence.

To examine this synergy sequence quantitatively, Figs. 2d and 3b were obtained in identical fashion to Figs. 2b, 3a for the NMDA data (method illustrated in Fig. 2a). The individual frogs ($n = 4$, identified in Fig. 2d), all showed the A–B–G–A–F–E+G sequence during the step cycle, but one frog (f10) rarely showed synergy G

Fig. 2 Synergy sequence in individual NMDA-evoked caudal extension-lateral force-flexion cycles, and step cycles. **a** Method of determining period of synergy activations. The caudal-lateral extension and flexion phase are each divided in five responses (1–5, 6–10). Synergy A, B, G, F, and E activations are shown, with each synergy maximum at 100 %. *Boxes* indicate periods of activity above 70 % threshold *dotted line*. *Box* height in each bin is determined by the relative order from most to least-activated synergies above that threshold (height of four empirical units for the most active synergy, e.g., *box A* height is ¾ of *box B* in response 1, and *box G* height is ½ of *boxes F* and E in response eight, considered ex-aequo with <5 % difference). **b** Timing of synergies A, B, G, F, and E. For each cycle, the weighted centers of the *boxes* from **a** are *plotted* as the times of synergy activity, with synergy-specific symbols. Abscissa is response in the cycle. *Cycle* shown in **a** is cycle 2. *Lines* joining symbols indicate each synergy main periods of activity across cycles. A few outliers are not joined to the *lines*. We generally note an A+B–G–A–F–E–G synergy sequence. **c** Example of a step cycle. Stance and swing are each divided in five equal intervals (1–5, 6–10). EMGs are reconstructed with the NMDA synergies of Fig. 1b. Synergy A, B, G, F, and E activations are shown, with each synergy maximum at 100 %. Observed and reconstructed EMG responses shown as solid and dashed lines joining the average rectified EMG value at the mid-time of each parsed response. The reconstruction R^2 was 0.76. **d** Timing of synergies A, B, G, F, and E in 173 steps. *Boxes* weighted centers representing synergy activations above 70 % threshold in traces such as at Fig. 2c *bottom,* were *plotted* as the times of synergy activity for each step. Abscissa is step response. *Lines* joining *symbols* indicate each synergy main periods of activity across cycles. A few outliers are not joined to the *lines*. We generally note an A–B–G–A–F–E+G synergy sequence. The four *stepping frogs* are indicated near the ordinate
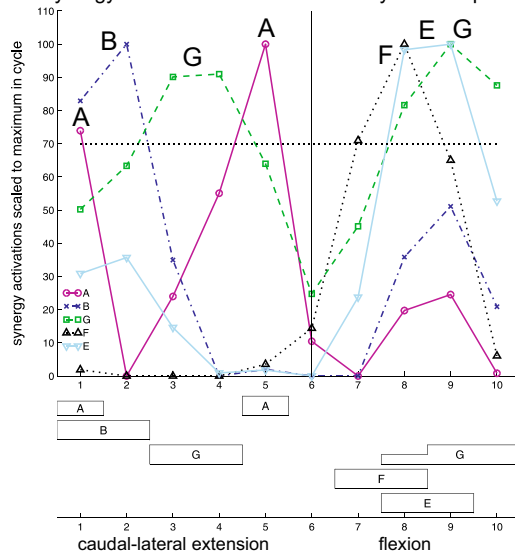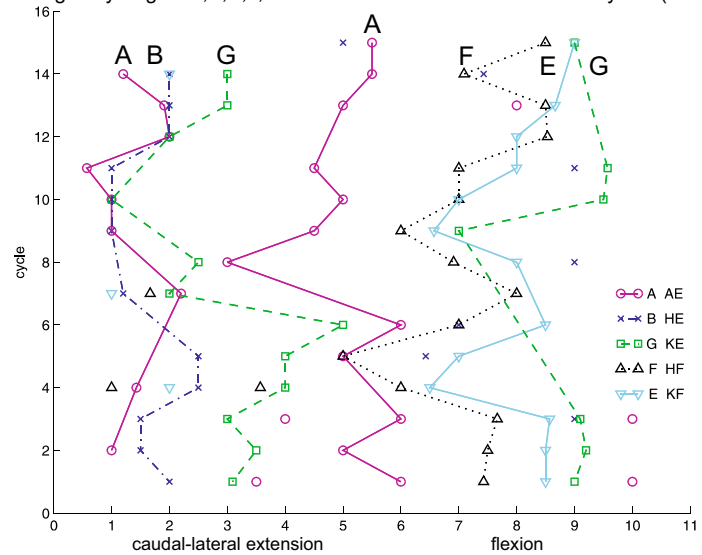
activation during swing, and had no clear separation between the timing of synergy B and G activation during stance. The angular histograms of the distribution and means of timing of synergy activations are plotted with or without f10 in Fig. 3b. The differences in orientation between consecutive arrows were all statistically significant (Table 2). The results support the conclusion that the A–B–G–A–F–E+G synergy sequence is activated during the stance-swing cycle of locomotion. Comparison of Fig. 3a and b lower right histograms shows a very similar synergy sequence for locomotion and the NMDA caudal extension-lateral force-flexion cycle (synergy E activation occurs later during the flexion phase of locomotion).

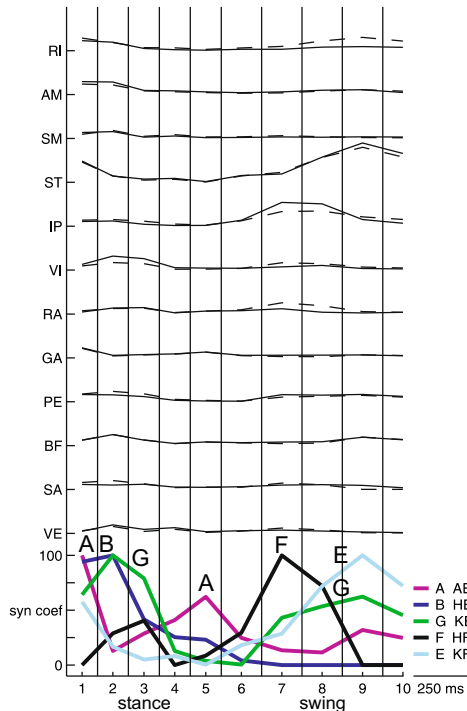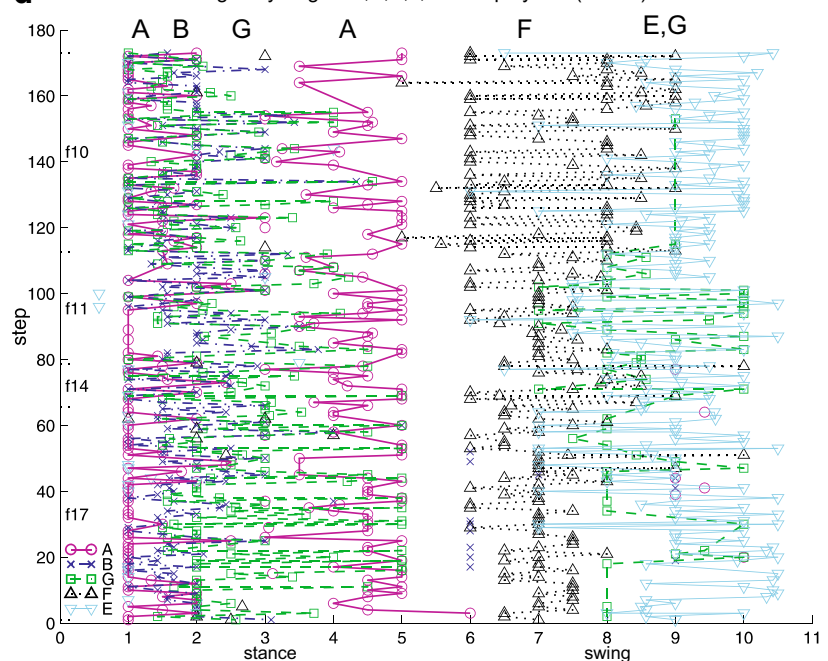## Comparison of NMDA caudal extension-lateral force-flexion and locomotor synergy sequence

This comparison can also be made by averaging the cycles of synergy activation, such as the one shown in Fig. 2a. Figure 4a is the average of the 15 NMDA caudal extension-lateral force-flexion cycles analyzed in Figs. 2b, 3a, and 4b the average of the 173 step cycles analyzed in Figs. 2d, 3b. No threshold is used in that method. The A–B–G–A–F–E–G synergy sequence can again be identified in both averages.

In Fig. 4a, synergy G outlasts B during the extension phase (G > B in responses 3–5, $P = .0098, .0002, .0104,$

NMDA-evoked synergy sequence A-B-G-A-F-E-G

a 70 percent threshold method to determine timing of synergy activations in an individual cycle example

b timing of synergies A,B,G,F,E in caudal-lateral extension-flexion cycles (n=15)
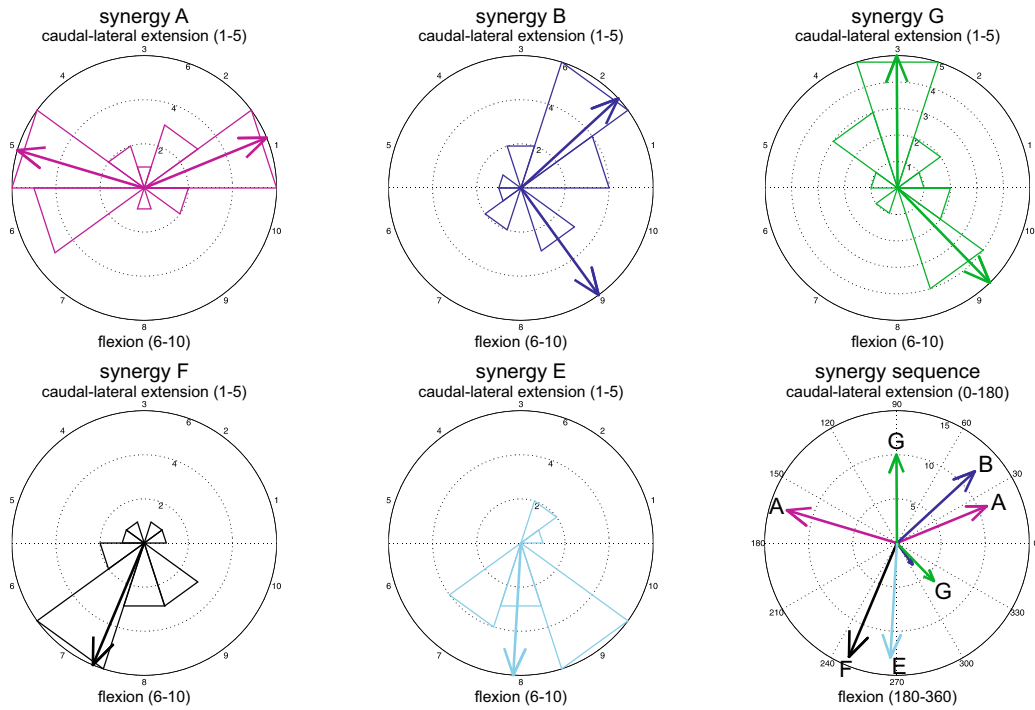

Locomotor cycle synergy sequence A-B-G-A-F-E+G

c reconstruction of a step with NMDA synergies

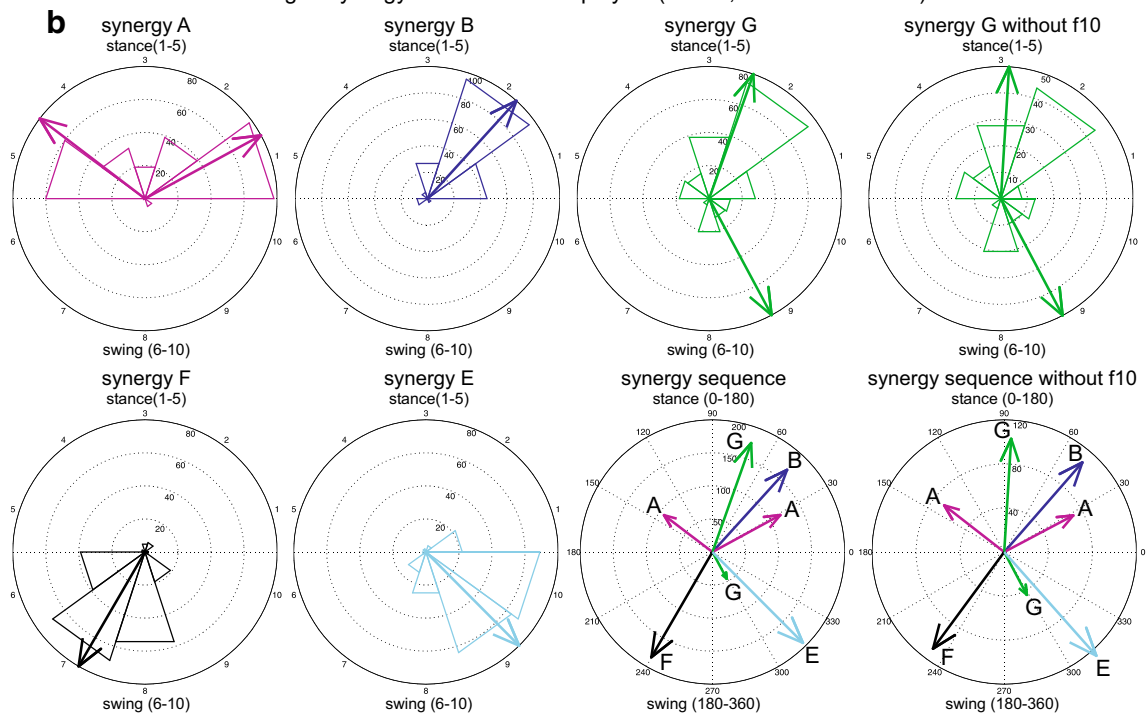**d** timing of synergies A,B,G,F,E in step cycles (n=173)

one-tailed unpaired t tests, df 28). The second synergy A peak outlasts G (A > G in response five, $P = .0041$, df 28), and is followed by synergy F, which precedes synergy E (F > E in responses 6–7, $P = .0042, .0265$, df 28). Synergy G follows in late flexion. In Fig. 4b, synergy G outlasts B during stance (G > B in responses 3–5, $P < 10^{-5}$, $< 10^{-10}$, $= 10^{-8}$, 1-tailed unpaired t tests, df 344). Synergy A peaks

twice, in early and late stance. The second synergy A peak outlasts B and G (A > B in responses 3–5, $P < 10^{-4}$, $= 0, 0$; A > G in responses 4–5, $P < 10^{-8}$, $=0$, df 344), and is accompanied in late stance by synergy F, which abruptly increases in early swing. Synergy E follows synergy F (F > E in responses 6–8, $P = 0, 0, .036$; E > F in responses 9–10, $P = 0, 0$, df 344), and precedes synergy G.

a Timing of synergy activations in NMDA-evoked caudal-lateral extension-flexion cycles (n=15)

Timing of synergy activations in step cycle (n=173; n=112 without f10)

◀ **Fig. 3** Synergy sequence in NMDA-evoked caudal extension-lateral force-flexion cycle, and in locomotion. **a** Distribution of synergies A, B, G, F, and E activations in the NMDA cycle. *Timings* shown in Fig. 2b are plotted in *circular histograms* (e.g., values >0.5 and <1.5, ≥1.5 and <2.5, and ≥9.5 and ≤10.5 in bins 1, 2 and 10, labeled on periphery). *Number* of observations indicated inside *concentric circles*. *Arrows* indicate the time of synergy activation peaks, computed as averages of values in bins 10 and 1–2, and bins 4–6 for synergy A; bins 1–3, and bin 9 for synergy B; bins 2–4, and bins 9–10 for synergy G; bins 6–9 for synergy F; and bins 7–9 for synergy E. All synergy activation peaks are plotted together in the *lower right histogram*, with a length equal to the number of values averaged to obtain each peak. **b** Distribution of synergies A, B, G, F, and E activations in the step cycle. Analysis and display are similar to those of **a** for the NMDA cycles. Timings shown in Fig. 2d are *plotted* in *circular histograms* (bins 1–5, stance, and bins 6–10, swing), with or without f10 steps in the case of synergy G. *Number* of observations indicated inside *concentric circles*. *Arrows* indicate the time of synergy activation peaks, computed as averages of values in bins 1–2, and bins 4–5 for synergy A; bins 1–3 for synergy B; bins 1–5, and bins 8–10 for synergy G (bins 2–5 and bins 8–10 without f10); bins 6–9 for synergy F; and bins 7–10 and 1 for synergy E. All synergy activation peaks are *plotted* together in the *lower right histograms*, with a length equal to the number of values averaged to obtain each peak

Table 1 Comparisons of mean phase of synergy activations in NMDA-evoked caudal extension-lateral force-flexion cycle (Fig. 3a, lower right)

Synergy activation phase	P value	Degrees of freedom
B versus A	0.0255*	21
G versus B	4.2×10^{-5}**	20
AA versus G	10^{-6}**	21
F versus AA	3×10^{-8}**	25
E versus F	0.0528	25
GG versus E	9.4×10^{-4}**	17
A versus GG	1.2×10^{-5}**	15

AA and GG refer to the second synergy A and G peaks in the cycle, which begins with the caudal-lateral extension phase and ends with the flexion phase (Fig. 3a, lower right)

* $P < .05$, ** $P < .005$

In summary, the averages of Fig. 4 and the statistical tests comparing the temporal course of synergy activations, support the results of the previous analyses showing a similar A–B–G–A–F–E–G synergy sequence in the NMDA caudal extension-lateral force-flexion, and locomotion cycles.

Synergy topography

The question of whether there is a topographic organization of synergies in the spinal cord is by itself of interest, and also relevant to determine how the synergy sequence identified in the previous sections may be generated.

Table 2 Comparisons of mean phase of synergy activations in locomotion (Fig. 3b, lower right, all frogs)

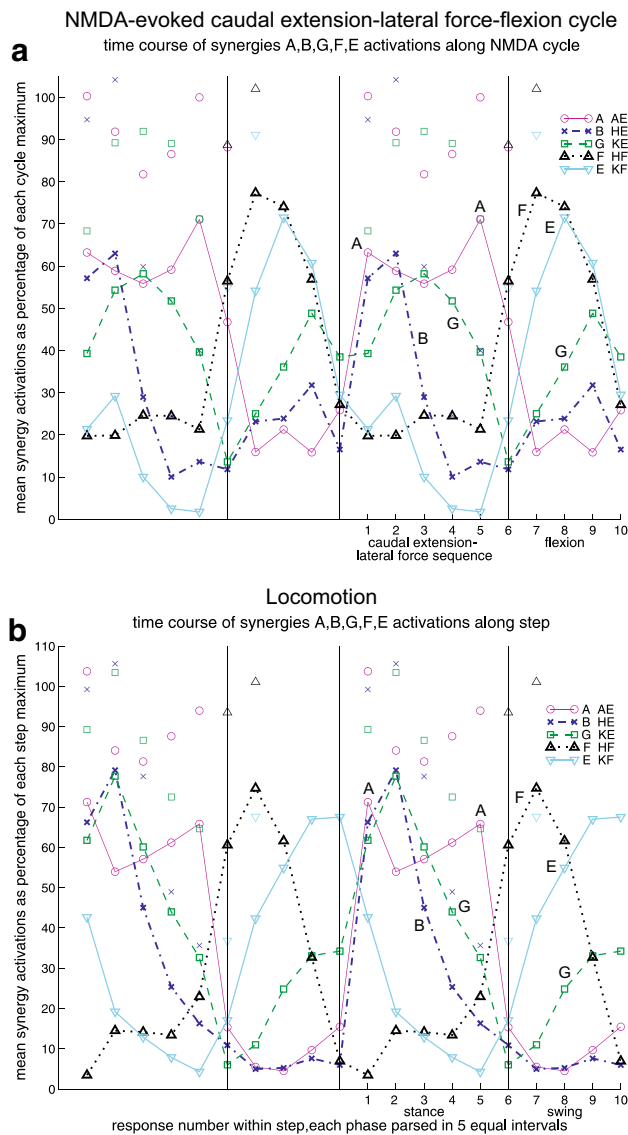| Synergy activation phase	P value	Degrees of freedom
B versus A	2×10^{-14}**	283
G versus B	4×10^{-10}**	341
AA versus G	0**	265
F versus AA	0**	274
GG versus F	0**	228
E versus F	0**	376
GG versus E	.045**	238
A versus GG	0**	161
A versus E	0**	309

AA and GG refer to the second synergy A and G peaks in the step cycle, which begins with stance and ends with swing (Fig. 3b, lower right)

** $P < .005$

Figure 5a shows a map of all active ($n = 110$, red circles) and silent sites ($n = 292$, black x) to NMDA, and a map of the closest active and silent sites in each dorsoventral track ($n = 70$) that contained both an active and a silent site. In these tracks, the average distance between the active and silent site was 250 ± 100 μm ($n = 70$). It is seen that the lumbar cord was rather homogeneously sampled, and that the active sites were generally located at an intermediate depth (947 ± 224 μm, cord diameter 2000 μm).
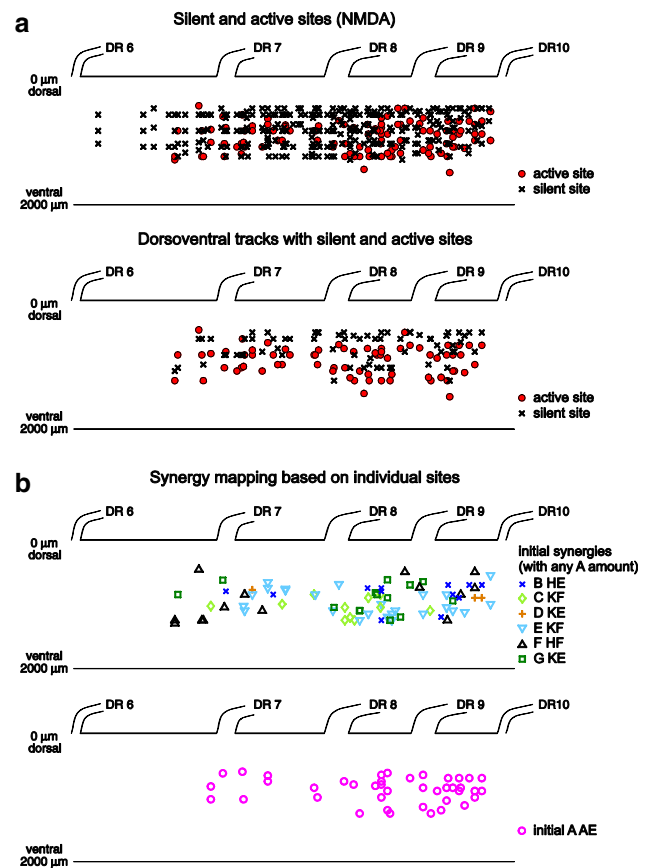
Figure 5b shows two-dimensional maps (rostrocaudal location and depth) of the individual spinal sites encoding muscle synergies. Because synergy A was a predominant synergy in the output (see Fig. 6a), any amount of synergy A was allowed when defining a synergy B, C, D, E, F or G encoding site (see "Materials and methods"). These maps show two foci of synergy F in the rostral and caudal ends of the lumbar cord; a focus of synergy C in the upper part of 8–9th segment; two foci of synergy B below the 8th root, and a few rostral synergy B sites; a focus of synergy G in the 8th–9th segment. Synergy E is more diffusely distributed, but is clearly seen to begin caudally to the rostral focus of synergy F. Synergy A has a rather widespread distribution, with in particular caudal foci overlapping those of synergy B.

Figure 6 shows the rostrocaudal topography of the seven synergies in the spinal cord divided in 10 bins. In the left column, topography is based on the initial responses evoked by NMDA at 110 sites. In the right column, topography is based on the subsequent (second to tenth) responses evoked by NMDA. Several points can be made. First, similar to Fig. 5b, each synergy is preferentially evoked from certain cord regions, which are often multiple for a given synergy, and frequently overlap with those of

Fig. 4 Comparison of the synergy sequence in the NMDA-evoked caudal extension-lateral force-flexion cycle, and locomotion. **a** Average of the 15 NMDA cycles of Figs. 2b, 3a (one such cycle shown in Fig. 2a). Extension and flexion phases each divided in five equal intervals (1–5, 6–10 on abscissa). The average is shown twice side-by-side to better visualize the phase transitions. **b** Average of the 173 step cycles of Figs. 2d, 3b (one such cycle shown in Fig. 2c). Stance and *swing* phases each divided into five equal intervals (1–10). The synergy sequence A–B–G–A–F–E–G is seen in both averages. *Symbols* above traces represent one standard deviation

other synergies. Table 3 (left) shows that there is a significant difference in activation between the 10 bins, for all synergies except synergy E according to parametric testing (ANOVA), and for all 7 synergies with nonparametric testing (Mack–Skillings). Table 3 (right) also shows that post hoc Scheffé tests comparing the activation between bins of higher and lower average activation across the ten responses are statistically significant in both parametric and
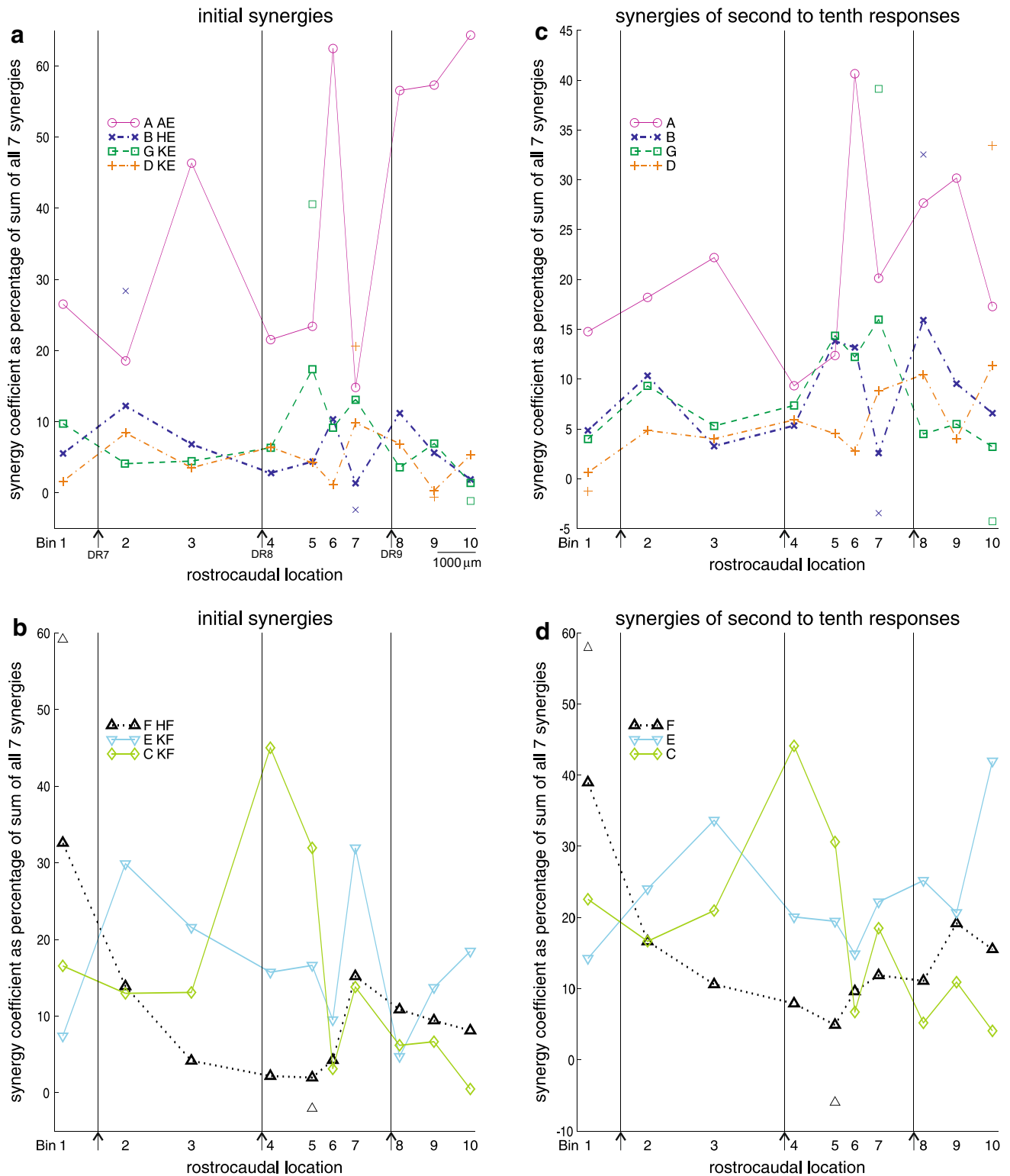

Fig. 5 Spinal cord maps of active and silent sites, and of individual sites encoding synergies A to G. **a** Location of active spinal sites (*red circles*) and silent sites (*black x*) to NMDA iontophoresis in ten frogs. *Upper panel*: the 110 active sites and 292 silent sites are all shown. *Lower panel*: closest active and silent sites belonging to the same dorsoventral tracks (n = 70). **b** Location of individual spinal sites encoding muscle synergies. *Upper panel*: sites encoding synergies B, C, D, E, F or G are shown with *different symbols*. A site was considered to encode one of these six synergies when the activation of that synergy in the initial responses exceeded each of the other five synergies by a ratio ≥1.733 (arctangent ≤ 30°). Any amount of synergy A was allowed. *Lower panel*: sites encoding synergy A. Its activity in the initial responses exceeded each of the other six synergies by a ratio ≥1.733

Fig. 6 Spinal cord rostrocaudal topography of synergies A–G. **a**, ▶ **b** Rostrocaudal topography of A, B, G, and D extensor synergies (**a**), and of F, E, and C flexor synergies (**b**), based on the initial NMDA responses. 110 sites were divided rostrocaudally in 10 bins. For each bin, the percentage contributions of synergies A–G to the initial responses at each site were averaged, and *plotted* at their mean location. *Symbols* above and below traces represent one standard deviation (SD), shown at bins where synergies B, G, D, and F were most and least active. SDs were 33.4 and 23.9 % at bins 10 and 7 for synergy A, 45.1 and 1 % at bins 4 and 10 for synergy C, and 36.8 and 7.1 % at bins 7 and 8 for synergy E. *Numbers* identify the bin centers, and *arrows* the middle of dorsal roots 7, 8, and 9. **c**, **d** Rostrocaudal topography of synergies A–G based on the second to tenth set of responses in the NMDA-evoked output. For each bin, the percentages that synergies A–G contributed to the second to tenth set of responses at each site were pooled together, averaged, and plotted. SDs were 35.5 and 17.5 % at bins 6 and 4 for synergy A, 32 and 7.3 % at bins 4 and 10 for synergy C, and 35.2 and 13.8 % at bins 10 and 1 for synergy E

Synergy topography in the spinal cord

a initial synergies

b initial synergies

c synergies of second to tenth responses

d synergies of second to tenth responses

nonparametric testing. This is true even for synergies whose peaks of highest activation are less prominent (extensor synergies B, G, D). Second, in general extensor

synergies and flexor synergies (top and bottom rows of Fig. 6) are preferentially activated caudally and rostrally to one-third of the DR8–DR9 segment, respectively (an

Table 3 Synergy rostrocaudal topography (110 sites in 10 bins; based on 1st to 10th NMDA responses)

Two-way mixed-design ANOVA

Synergy	P values of omnibus F test (ANOVA)			Post hoc contrast between groups of bins with higher versus lower activations (Scheffé)		
	Location (bin)	Time (responses)	Location × time	Higher bins	Lower bins	P value
A	0.0053*	8.7×10^{-9}*	0.144	6, 8–9	1, 4–5	.0355*
B	0.0358*	0.240	0.033*	5–6, 8	1, 3, 7	.0713+
C	0.0002*	2.2×10^{-7}*	0.277	4–5	6, 8–10	.0020*
D	0.0243*	0.639	0.998	7–8, 10	1, 6, 9	.0561+
E	0.343	0.049*	0.861			
F	0.00004*	8.7×10^{-7}*	0.364	1–2, 9–10	3–6	.0382*
G	0.0194*	0.878	0.610	5–7	1, 8, 10	.0350*

Nonparametric Mack–Skillings

Synergy	P values of Mack–Skillings rank test	Post hoc pairwise comparisons between individual bins with high versus low activation (Scheffé)		
	Location (bin)	Higher bin	Lower bin	P value range
A	0*	6, 8 or 9	4 or 5	6×10^{-4}–10^{-11}*
B	0*	5, 6 or 8	1, 3 or 7	1.5×10^{-5}–.0237*
C	0*	1, 3, 4 or 5	6, 8, 9 or 10	0–.0078*
D	1.3×10^{-14}*	7 or 8	1 or 6	5.6×10^{-9}–.0131*
E	10^{-8}*	3 or 10	1 or 6	.0015–.0085*
F	0*	1	Any of 2–10	0–2×10^{-7}*
G	0*	5, 6 or 7	1 or 10	10^{-8}–.0042*

Synergy topography examined with two statistical methods: two-way mixed design ANOVA with one independent factor (bin location, numbered 1–10 rostrocaudally) and one repeated-measurements factor (the 1st–10th set of NMDA responses at each site); and nonparametric Mack–Skillings rank test on bin location. Both analyses were followed by post hoc Scheffé tests comparing bins with higher and lower activations of the different synergies, tested as complex contrasts after ANOVA, and as pairwise comparisons after Mack–Skillings

* $P < .05$, + $P < .1$. ANOVA F tests degrees of freedom location (9, 86), time (9, 797), location x time (81, 797), post hoc contrasts (9, 86); Mack–Skillings Chi-square degrees of freedom location (9) and pairwise comparisons (9)

exception is synergy E with both strong rostral and caudal representations). Third, certain features of the topography show a spatial synergy sequence reminiscent of the temporal synergy sequence A–B–G–A–F–E–G described above. For example, A and B show peaks of activation in bin 6, G in bin 7, A in bins 8–10, and then returning to the rostral end of the spinal cord and moving rostrocaudally again, F in bin 1, E in bin 2, G in bin 5 (an exception is the representation of synergy B in bin 8, with no match in the temporal sequence). Fourth, while the topographies based on the second to tenth responses and on initial responses are generally similar, indicating robustness, there are also some interesting differences that may again suggest a rostrocaudal sequential activation of synergies. For example, in the initial responses, bins 5, 6, 7 show activation peaks for synergies G, B, G, respectively (Fig. 6a). But in later responses, bin 5 also shows an activation peak for B, and bin 6 for G (Fig. 6c). Although only suggestive, this is

compatible with the idea that by the time of the later responses, activity has spread rostrocaudally from bins 5 and 6 to bins 6 and 7, so that later responses evoked from bins 5 and 6 resemble the initial responses evoked by bins 6 and 7. Similarly the amount of synergy A produced by bins 8–10 decreases in the later compared to the initial responses (Fig. 6c versus a), whereas the amount of synergy F evoked by bins 9–10 and E by bin 10 increases (Fig. 6d versus b). Thus, bins 9 and 10 show in the later responses, synergies evoked by bins 1 and 2 in the initial responses, another example of continuity if we assume as above that the caudal-most part of the cord (bin 10) next relates to the rostral-most part of the lumbar cord (bin 1).

In summary, a distinct although overlapping topography of synergies exists in the cord. The rostrocaudal spatial disposition of synergies in the cord appears to mirror the temporal synergy sequence identified earlier in the paper. The comparison of topography based on initial and later
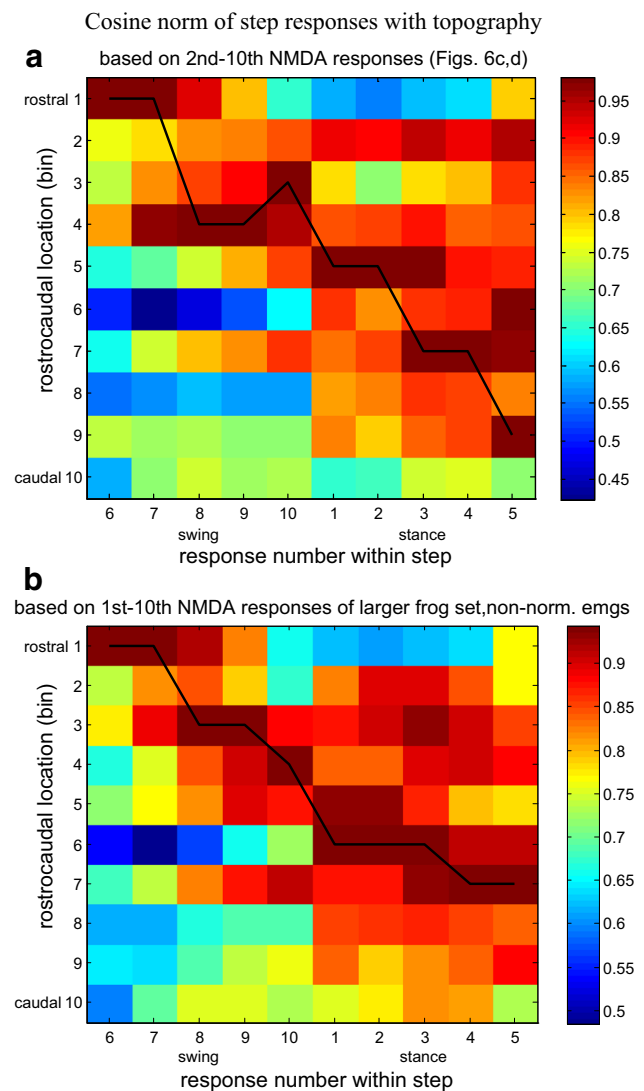
NMDA-evoked responses also hints at the synergy temporal sequence being constructed by activation of spatially adjacent synergy representations.

Comparison of locomotor synergy sequence and synergy topography

The previous section suggested a similar order in the locomotor synergy sequence and the rostrocaudal synergy topography in the spinal cord.

To evaluate this quantitatively, we computed the normalized dot product between the average synergy composition of each response of the step cycle (responses 1–5 in stance, 6–10 in swing) and the average synergy composition evoked by each bin (bins 1–10 rostrocaudally) of the topography. The average locomotion and topography synergy compositions were determined in the same way. In each response of an individual step cycle or at each spinal cord site, activations of synergies A to G were expressed as a percentage to a sum of 100, to ensure that the balance of synergies is taken into account. We then computed the average synergy compositions of responses 1–10 of the step cycle, and of bins 1–10 of the topography. Finally each synergy average was normalized to a value of 100 % at its maximum in the step cycle or the topography. This ensured that each synergy is equally considered, with its distribution of peaks and troughs in the topography, for its recruitment in the construction of the step cycle. Figure 7a shows the result of this analysis using the synergy topography of Fig. 6c, d. As we proceed from early swing to late stance, the synergy composition best matches with generally progressively more caudal locations in the spinal cord (black line joining the hottest squares on the color scale). These results are confirmed in Fig. 7b, when we added an earlier set of 12 frogs, with topography now based on 168 sites from 22 frogs, the first to tenth responses evoked by NMDA at each site, and non-normalized NMDA EMGs (same as for locomotion).

To quantify the rostrocaudal trajectory of the traveling wave in Fig. 7a and b (black lines), we computed the Pearson linear correlation coefficients between the rostrocaudal location (bin number) whose synergy composition best matches the successive step responses of the swing–stance cycle, and these step responses (renumbered from 1 to 10). These coefficients were 0.9491, and 0.9653, respectively. By comparison, when we randomly shuffled the spinal cord sites locations, and did the same analyses as in Fig. 7a and b, only 0.25 and 0.06 % of 10,000 site-shuffled simulations gave higher correlation coefficients than the ones observed with our data. This suggests that the observed synergy topography in the spinal cord crucially underlies the finding of a rostrocaudal traveling wave in locomotion.

Fig. 7 Comparison between the synergy composition of successive responses in the step cycle, and synergy rostrocaudal topography. **a** Cosine angle between the average synergy composition of step responses (6–10, swing, and 1–5, stance), and the 10 bins synergy topography based on the second to tenth NMDA responses (Fig. 6c, d). In contrast to Fig. 4b, each step response had its seven synergy coefficients summing to 100 %, before averaging each of the 10 responses across the 173 steps. This represents an identical treatment to that used for topography (Fig. 6). Next, for each synergy, the step response or the bin with the highest average activation was given a value of 100 %, and the other step response or bin values scaled accordingly. We then computed the normalized dot products between the 7-synergy vector of each step response and the 7-synergy vectors for each rostrocaudal bin, and plotted them in pseudocolor. The black line joins the highest matches between the step responses and the synergy topography (highest cosine angle). **b** Similar analysis, but with the topography based on non-normalized NMDA EMGs (same as for locomotion), the first to tenth NMDA responses, and an additional 12 frogs (total of 168 sites). Together, both *plots* suggest a rostrocaudal progression of activity along the step cycle

The activity is not necessarily restricted to a single focus in the cord at each phase of the step cycle, since the synergy composition of stance responses also matches to a

lesser extent than caudally, that of some more rostral bins in the cord. Processing the locomotion data slightly differently so that normalized dot products (ndp) were first computed between the responses of each individual step and the topography before averaging (see "Materials and methods") gave similar results to Fig. 7a, b, but allowed to do statistics. Paired t tests showed that for each stance response 1–5, its highest ndp (best-matching topographic bin among bins 1–10, black line in Fig. 7) was significantly greater than its highest ndp with rostral bins 1–4 ($P < .02$, range 0–0.0112, df 172).

In summary, Fig. 7a, b suggests that the step cycle may be constructed from swing to stance through progressively more caudal activations in the lumbar cord. A rough estimate of the average speed of the traveling wave, based on a 16.55 mm distance between the 6th and 10th dorsal roots, and average locomotor cycle duration of 1363 ± 432 ms ($n = 173$) would be 12 mm/s.

Discussion

In this paper, we find that locomotion consists of a synergy activation sequence (A–B–G–A–F–E–G). The same sequence is obtained when focal spinal NMDA iontophoresis elicits a caudal extension-lateral force-flexion cycle (flexion onset without synergy C). The NMDA method also reveals a rostrocaudal topographic organization of synergy encoding by the lumbar cord. Each synergy is preferentially activated from distinct regions, partially overlapping between different synergies. Comparing the locomotor synergy sequence with the spinal cord synergy topography suggests that locomotion is achieved by a rostrocaudally traveling wave of activation.

Sequence of synergies

Locomotion requires the medulla, but shares synergies with the spinal cord (Roh et al. 2011). Our finding that despite an imperfect reconstruction of locomotion with NMDA-identified spinal synergies ($R^2 = 0.73$), the spinal cord can produce a caudal extension-lateral force-flexion rhythm with a similar synergy sequence to locomotion (Figs. 2, 3, 4) supports this conclusion.

The frog stance A–B–G–A synergy sequence (Fig. 4) is a simultaneous onset of ankle, hip, and knee extensor synergies (A, B, and G), later offset of knee extensor, and a second ankle extensor synergy peak in late stance, similarly to cat locomotion (Krouchev et al. 2006; Markin et al. 2012). A late stance human ankle extensor synergy peak also occurs (Chvatal and Ting 2012). The frog swing F–E–G synergy sequence (Fig. 4) activates in turn hip and knee flexor synergies (F activating mainly IP, RA, and E mainly

ST), before synergy G which includes PE, ankle flexor and knee extensor. Synergy F timing resembles that of cat RA and IP in late stance-early swing. Synergy E timing later in swing is alike the human knee flexor synergy, and one of two cat synergies activating ST. Synergy G timing in late swing is alike an ankle flexor synergy in the cat, and one of two ankle flexor synergy periods in the human. Thus, synergies with a specific function frequently have a similar timing in the frog compared to the cat and human.

Topography of synergies

Little is known about synergy topography. The rodent shows partial segregation mediolaterally of premotor neurons to extensors versus flexors (Puskàr and Antal 1997; Tripodi et al. 2011), and dorsoventrally of commissural neurons (Butt and Kiehn 2003). Optical stimulation of ventral glutamatergic neurons at L2 evokes flexor and at L5 extensor bursts (Hägglund et al. 2013). Individual motoneuron pools are monosynaptic targets of a premotor column in medial lamina V, believed to encode synergies, with evidence for a rostrocaudal topography (Levine et al. 2014).

In our study, given the greater rostral representation of flexor synergies F and E, and generally greater caudal representation of extensor synergies A, B, G, D (Figs. 5, 6), we find that although mixed, flexor interneurons predominate rostrally, and extensor interneurons caudally. This relates to in vitro locomotion results of a mixture of preferred interneuronal firing phases in each segment, but more often in phase with the segment output, flexor in L2, and extensor in L5 (Tresch and Kiehn 1999; Cheng et al. 2002; Kwan et al. 2010; Dougherty and Kiehn 2010; Zhong et al. 2010, but see Auyong et al. 2011; Antri et al. 2011; Hinckley and Pfaff 2013, who found no correlation between firing phase and rostrocaudal location). The overlap of the preferred zones of activation of different synergies in Figs. 5, 6 is expected since an only partial segregation is the rule in spinal interneuronal systems (Jankowska 2008; Levine et al. 2012).

Many synergies are represented more than once, unlike motoneurons. Thus, unlike the F hip flexor and A ankle extensor synergies, hip flexor and ankle extensor motoneurons have single rostrocaudal representations (Cruce 1974). Multiple representations afford many possible synergy combinations and sequences, as a given synergy will have different overlapping and neighboring synergies in its different representations. Thus, synergies A and B in bins 6 and 8 (Fig. 6a) may help to construct the A+B combination, and A in bins 8–9 (Fig. 6c) and F in bins 9–10 (Fig. 6d) the A–F sequence. Using patchy redundant somatotopy to construct movement had been suggested for spinal cord (Székely and Czéh 1971) and cortex (Klein Breteler et al. 2007).

Traveling wave

Comparing the synergy sequence in locomotion with synergy topography suggests a rostrocaudal wave of activation (Fig. 7). Thus, the rostrocaudal CPG chains in the lamprey, fish and tadpole may in fact have been conserved in the locomotor CPG of limbed vertebrates (Cohen 1988).

Comparing EMG sequence and motoneuronal topography in cat and human locomotion (Yakovenko et al. 2002; Ivanenko et al. 2006a) suggested rostrocaudal activation with some abrupt shifts. In the rodent, rostrocaudal motoneuron activation was imaged (Bonnot et al. 2002; O'Donovan et al. 2008), and propagating waves were recorded in ventral roots (Cazalets 2005).

The only prior evidence of rostrocaudal interneuronal activation of the mammalian CPG is in fictive cat scratching (Cuellar et al. 2009), shown as a traveling wave of cord dorsum potentials persisting after ventral horn removal, and by interneuronal recordings. But AuYong et al. (2011) found no such wave in cat air-stepping, and the absent topography of preferred interneuronal firing phase in rat locomotion (Antri et al. 2011) argues against a wave. A majority of air-stepping neurons being active in late swing-early extension, and of neurons having no phase preference upon inspecting Antri et al. Fig. 2, perhaps made a wave harder to evaluate. Pérez et al. (2009) model of flexor and extensor half-centers at each rostrocaudal level suggests a wave remains compatible with several phase preferences of interneurons in a given segment.

Spinal cord traveling waves propagate slowly at 0.1–0.3 m/s (Cazalets 2005; Cuellar et al. 2009), or even at 5–15 mm/s (Falgairolle and Cazalets 2007; O'Donovan et al. 2008), similar to our 12 mm/s estimate. This slow conduction would reflect interactions between neighboring oscillators, although longer propriospinal connections may participate (Cazalets 2005).

The locomotor CPG may consist of a timing structure and pattern formation network (Lennard 1985; Burke et al. 2001; Ivanenko et al. 2004; Saltiel and Rossignol 2004a, b; Rybak et al. 2006; Zhong et al. 2012). In scratching, the traveling wave keeps time during EMG deletions (Pérez et al. 2009). In locomotion, the traveling wave may underlie the temporal structure, and the interneuronal regions encoding synergies, pattern formation. In reaching, the same program unfolding in time for all directions (Churchland et al. 2012) may be akin to the traveling wave.

In the caudal extension–adduction–flexion rhythm, distant half-centers seemed involved (Saltiel et al. 2005). Perhaps this is a different mechanism, or there may again be a traveling wave with some regions along its path not or weakly expressed in the output. Also longer range connectivity might activate or prime distant regions ahead of the main wavefront of a traveling wave.

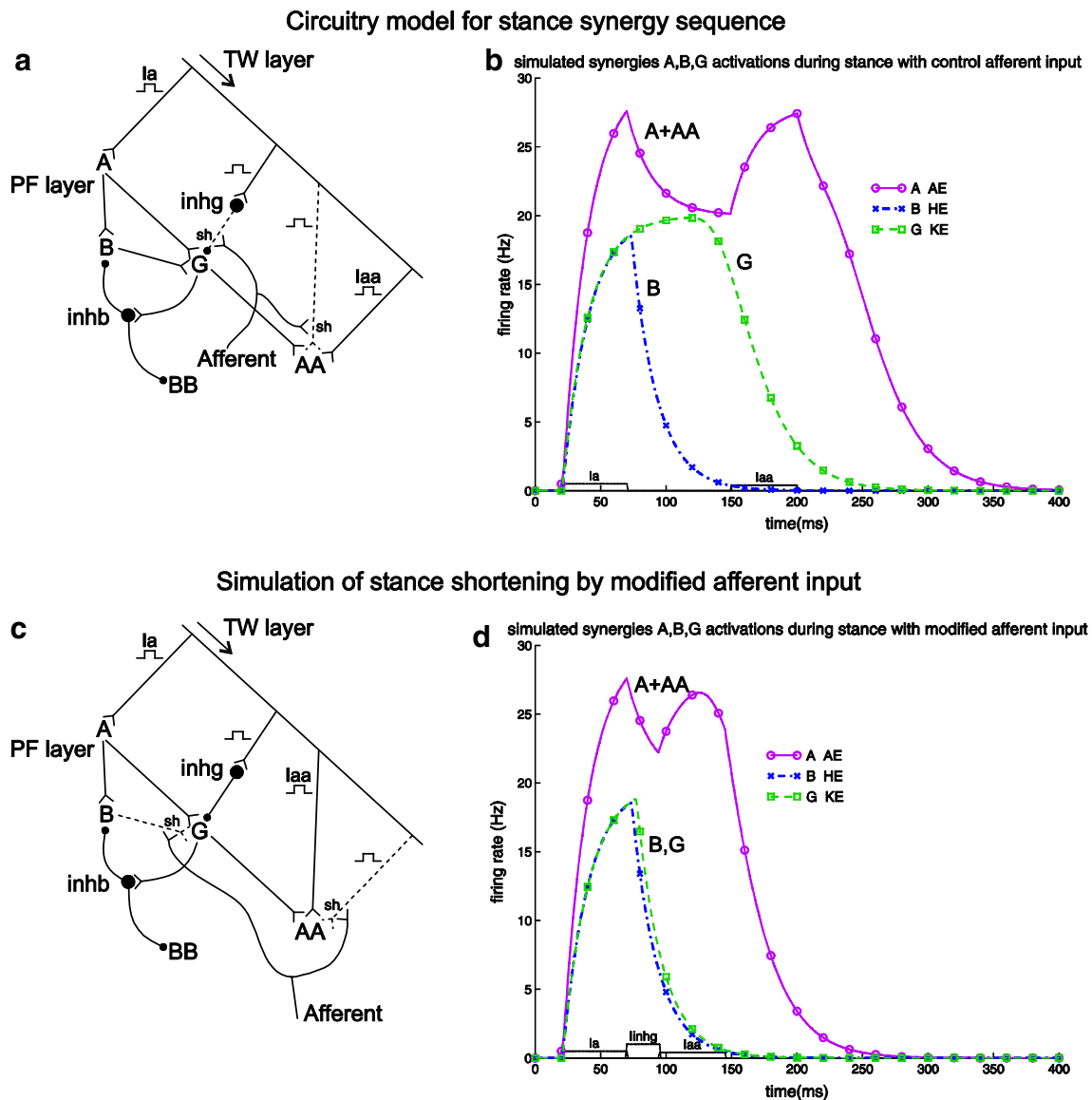## Simulations of stance synergy sequence, and of full cycle synergy sequence

Figure 8a circuit reproduces the A+B–G–A stance/extension synergy sequence of Fig. 4. It has three elements: a mixed-feed-forward-feedback loop (interconnections between A, B and G); a traveling wave (TW) layer providing Li's (2008) equations external inputs to the pattern formation (PF) layer; and afferent inputs to reconfigure the circuit. The external input to A triggers the synergy sequence (Fig. 8b) through the PF layer connectivity, but a properly timed external input to AA (Iaa) is needed to get the late synergy A peak. In Fig. 8c, afferents shunt the B to G instead of the inhg to G connection, so that G no longer outlasts B, while the PF layer connectivity automatically results in earlier synergy A inactivation (Fig. 8d). Afferents select between two possible external inputs from the TW layer to AA (full versus dashed line in Fig. 8a, c) to get the second synergy A peak appropriately timed (later in Fig. 8b and earlier in Fig. 8d).

Figure 9a circuit reproduces the A+B–G–A–F–E–G step/NMDA cycle synergy sequence of Fig. 4, and next ½ cycle (Fig. 9b). TW layer inputs to A2 and AA2 (2nd cycle) each arise at two possible times, and one of the inputs to A2 may instead activate E. Afferents control the effective inputs. In our simulations, the timing of the TW layer input to A2 solely determines the onset of activity in A2, B2, G2, and AA2, all signaling stance onset (Fig. 9b), while both the TW layer input to A2, and the PF layer circuitry are essential to obtain the first synergy A peak in the A2+AA2 curve. The TW layer input to AA2 is essential to the second synergy A peak.

In Fig. 9c, the external input to E, and the latter of the two possible TW layer inputs to A2 and AA2 are effective. The result is increased amplitude and duration of E and the swing phase (Fig. 9d). The following stance is delayed, but otherwise unmodified (compare Fig. 9b, d).

Unlike flexor–extensor half-center CPG models (McCrea and Rybak 2008; Pérez et al. 2009; Zhong et al. 2012), our model takes into account sequencing within the flexor or extensor phases, and synergy topography. Its feed-forward loop portion resembles how Cowley et al. (2010) envisioned descending propriospinal connections subserving locomotion (their Fig. 4). Because the traveling wave is a novel result that seems relevant to the temporal structure of the step cycle, we compare our model to Ivanenko et al. (2004, 2006a, b) where the emphasis is on temporal components at specific times in the step cycle. These were generally preserved across different forms of locomotion, with EMG differences attributed to changes in how a distribution network would channel the temporal pulses to motoneurons. It is not known, however, whether this network includes a limited set of muscle synergies such as
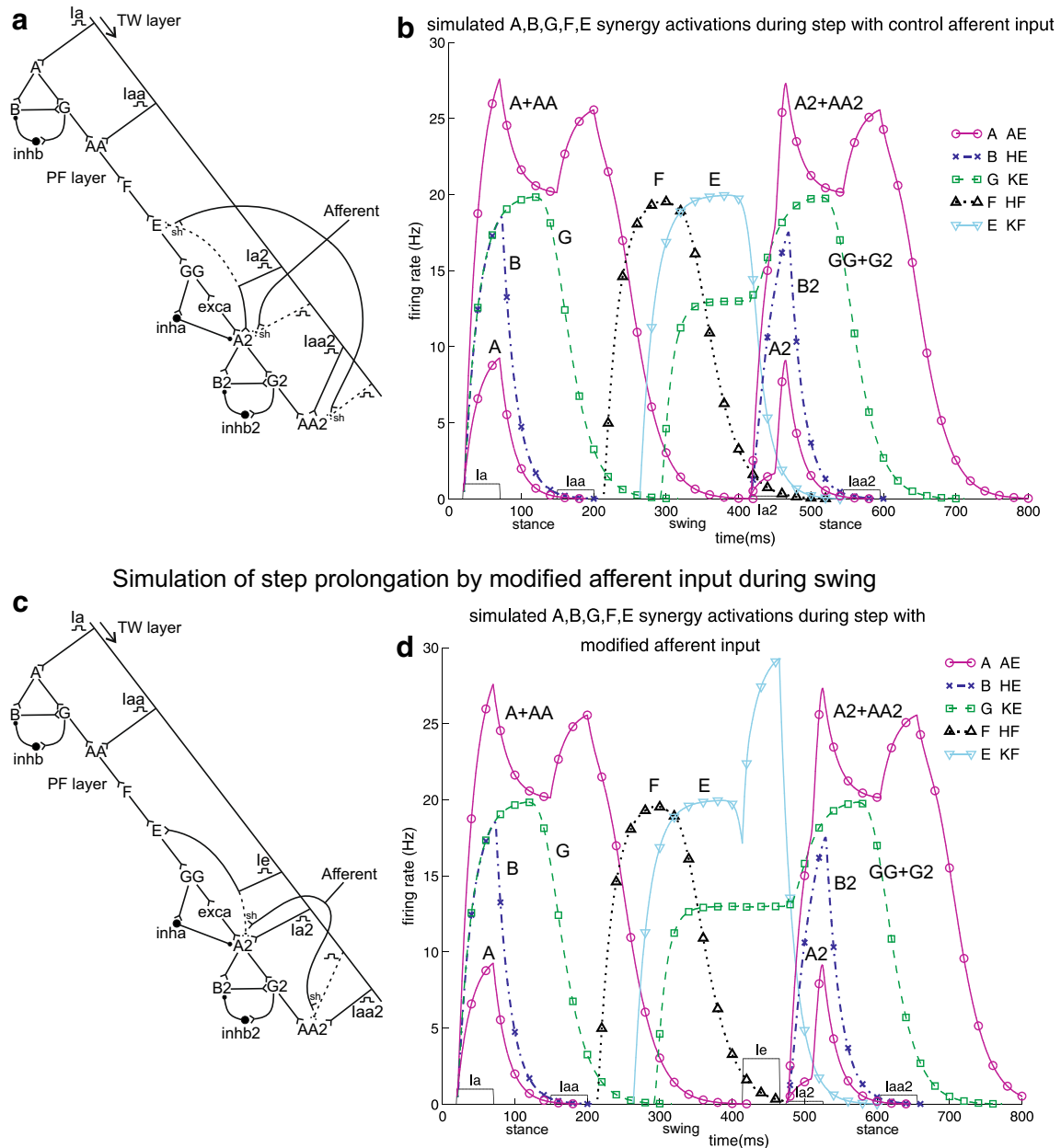
Circuitry model for stance synergy sequence

Simulation of stance shortening by modified afferent input

Fig. 8 Simulation of stance synergy sequence and its shortening by modified afferent input. **a** *Circuitry* model for regular stance synergy sequence. Capital letters represent synergy-encoding interneurons in the pattern formation (PF) layer (A, B, G, AA, and BB, where AA and BB are a second more caudal population encoding synergies A and B, corresponding to their respective topographic peaks in bins 8–9 and bin 8 in Fig. 6c); inhg and inhb are inhibitory interneurons. Excitatory and inhibitory connections are shown by a *fork* and *black circle*, respectively. The connection from inhb to BB is to account for the absence of a second B peak in the A+B–G–A synergy sequence. The *arrow* represents activity propagating rostrocaudally in the traveling wave (TW) layer, giving off branches that deliver brief pulses of activity with connectivity as shown. The pulse given to A initiates the sequence. In the model, afferents block impulse transmission in selective pathways through shunting presynaptic inhibition (sh, *dashed line*). In particular, two alternative pathways from the TW layer can activate AA at two different times, and this is under control

of the afferent input. **b** The A+B–G–A synergy sequence produced by the model in **a**, using Li equations and the parameters indicated in "Materials and methods". *Small rectangles* above the abscissa indicate the time of pulses delivery by the TW layer to A and AA (Ia and Iaa, corresponding to external inputs I_i in Li equations). **c** The same model as in **a**, except for a modified afferent input which now shunts a different set of pathways. The pathway from inhg to G, and the earlier *I*aa input to AA are now effective. **d** The synergy sequence produced by the model in **c**. The offset of synergy G is now no longer delayed with respect to synergy B. The second synergy A peak, and synergy A *offset* (A+AA curve) are advanced, and stance is shorter. Note that in the model, there is no interneuron population specifically responsible for the portion of synergy G activity (plateau) that is abolished in **d** versus **b**; rather, the G node in the model is responsible for the entire synergy G trace (*green dashed line* with *squares*) in both circumstances

ours. Also sequencing in their model appears solely determined by the temporal pulses, as no connectivity is postulated within the distribution network (PF) layer,

unlike in our model. Finally it is not known how their sequence of temporal pulses would arise, while our results suggest a traveling wave.

Circuitry model for step synergy sequence

Simulation of step prolongation by modified afferent input during swing

Fig. 9 Simulation of step synergy sequence and its prolongation by modified afferent input. **a** *Circuitry* model of step synergy sequence, and stance of the following step. *Capital letters* represent synergy-encoding interneurons in the pattern formation (PF) layer, and other conventions are the same as in Fig. 8. The suffix 2 corresponds to interneurons (A2, B2, G2, AA2, and inhb2), and external inputs (Ia2 and Iaa2) generating the following stance. Two alternative pathways from the traveling wave (TW) layer can activate A2 and AA2 in the PF layer with pulses at two possible times, under control of the afferent input. The more rostral external input from TW layer to A2 also has the potential to activate E, again under control of afferent input. The pulse given to A initiates the sequence. **b** The A+B–G–A–F–E–G synergy sequence, followed by A2+B2–G2–AA2 produced by the model in **a**, using Li equations and the parameters indicated in

Table 4. *Small rectangles* above the abscissa indicate the time of pulses delivery by the TW layer to A, AA, A2 and AA2 (Ia, Iaa, Ia2, Iaa2 correspond to external inputs I_i in Li equations). To better see these rectangles, their plotted amplitude is twice their actual value; and only activations >0.02 Hz are plotted in the synergy curves. **c** The same model as in **a**, except for a modified afferent input which now shunts a different set of pathways (sh, *dashed line*). The pathway to E (Ie), and the later (more caudal) Ia2 and Iaa2 inputs to A2 and AA2 are now effective. **d** The synergy sequence produced by the model in **c**. There is now a late increase in amplitude of synergy E activity resulting in prolongation of its activity, as well as that of the swing portion of the synergy G curve, due to GG. The onset of the subsequent stance is delayed, as determined by the later Ia2 input, but it otherwise proceeds normally

Table 4 Simulation parameters (Figs. 8, 9)

Neuron	τ (ms)	Thresh. T_i (Hz)	External input I_i (Fig. 8)		External input I_i (Fig. 9)	
			Control	Mod. affer.	Control	Mod. affer.
A	20	NA	0.5 Hz, 20–70 ms	0.5 Hz, 20–70 ms	0.5 Hz, 20–70 ms	0.5 Hz, 20–70 ms
B	20	0				
G	20	0				
inhb	20	17				
inhg	20	NA	(Effect on G shunted)	1 Hz, 70–95 ms		
AA	20	0	0.4 Hz, 150–200 ms	0.4 Hz, 95–145 ms	0.3 Hz, 150–200 ms	0.3 Hz, 150–200 ms
F	20	$5065e^{-k/40}$–1.7				
E	20	$12{,}250e^{-k/40}$+1.1				1.5 Hz, 415–465 ms
GG	13	15				
exca	20	0				
inha	20	3				
A2	20	9.8			0.1 Hz, 415–465 ms	0.1 Hz, 475–525 ms
B2	20	0				
G2	20	0				
inhb2	20	17				
AA2	20	0			0.3 Hz, 545–595 ms	0.3 Hz, 605–655 ms

External inputs shown are those that are effectively applied to A, AA, A2, AA2, E, or to G via inhg, depending on afferent input (see Figs. 8, 9)

τ time constant, *Thresh.* threshold, *k* iteration step in thresholds of neurons F and E, *NA* threshold is not relevant for neurons with only external inputs in Li equation, *mod. affer.* modified afferent input

Besides the two-layer structure, our model and Ivanenko's et al. do have similarities. Considered bilaterally, their temporal components reduce to three, in early stance, late stance, and early swing. In our model, the TW inputs to the PF layer are in early and late stance; while early swing is when the rostrocaudal wave begins rostrally (Fig. 7). The redirection of a TW input from A2 to E in Fig. 9a, c, and the two possible inputs to AA (Fig. 8) or AA2 (Fig. 9) resemble Ivanenko et al. network directing temporal components to different muscles, or perhaps premotor circuits. And a change restricted to the PF layer (shunting of B to G, Fig. 8b) being sufficient to change the output may also relate to reconfiguration in the distribution network of Ivanenko et al.

We have not detailed the TW layer circuitry and inputs to the PF layer, but interestingly Schneider (1992, 2003) reported layer III–IV neurons with an axon running ventrally, then giving longitudinal branches with intermittently spaced perpendicular collaterals. The idea of a tapped delay line is quite controversial (Rivest et al. 2010), but there is some evidence for it in the cerebellum (Freeman and Nicholson 1970; Cramer et al. 2013), and it has been modeled in the hippocampus (Zipser 1986). Selective presynaptic control of collaterals is documented (Lomeli et al. 1998; Rudomin 2002). Dorsal horn neurons producing spontaneous cord dorsum potentials, if coordinating the distribution of presynaptic inhibition effects (Manjarrez et al. 2003; Chávez et al. 2012), might be candidates for controlling transmission of inputs from the TW to PF layer.

In summary, our experimental method and analysis may complement other approaches investigating spinal cord circuitry. Our approach has been to dissect beyond just the extensor and flexor periods, the cycle of NMDA-focally evoked rhythms and of natural locomotion, focusing on synergy sequences; to investigate synergy topography; and to compare the two to formulate possible circuit connectivity for locomotion. Our results and simulations suggest that a rostrocaudally traveling wave of excitation takes advantage of the topography of interneuronal regions encoding synergies, to activate them in the proper sequence for locomotion.

Materials and methods

Surgery on frogs studied with NMDA

This part of the study represents new analyses on the same frogs ($n = 10$) as in our earlier papers (Saltiel et al. 2001, 2005). All procedures were approved by the Animal Care Committee at M.I.T. After anesthesia with 1 ml of 5 % ethyl 3-aminobenzoate methanesulfonic acid (Tricaine, Sigma–Aldrich) injected into the dorsal lymph sac, and ice, the frog (*Rana catesbeiana*) was spinalized at the obex. Twelve hind limb muscles were implanted: rectus internus (RI), adductor magnus (AM), semimembranosus (SM), semitendinosus (ST), iliopsoas (IP), vastus internus (VI), rectus anterior (RA), vastus externus (VE), biceps femoris (BF), sartorius (SA), gastrocnemius (GA), peroneus (PE). From individual muscles electrical stimulation (Loeb et al. 2000), RI and SM are hip extensor and knee flexor, AM hip extensor, ST primarily knee flexor, IP and RA hip flexor, VI and VE knee extensor, BF and SA hip flexor and knee flexor, GA knee flexor, but primarily plantar flexor (Cruce 1974), PE knee extensor and ankle dorsiflexor (Ecker 1971; Hulshof et al. 1987). After laminectomy, the dura and pia were opened ipsilaterally from the sixth to the tenth roots. A detailed drawing of the exposed spinal cord vasculature and dorsal root entry zones served to document the points of entry of the micropipette within each segment.

NMDA iontophoresis

NMDA was iontophoresed with a -100 nA current, till EMGs onset, or maximally 30 s, at depths around 500, 800 and 1100 µm, 200–400 µm from the midline. We previously showed this method reproducibility, estimated NMDA spread, and gave evidence that the NMDA effects represent interneuronal stimulation (Saltiel et al. 1998). The radius of spread should be 238 and 358 µm by the average onset of the first and last EMG responses used below to determine topography. These correspond to 5.7 and 12.8 % of the cross-sectional area (or 0.9 and 3.1 % of the volume) of an average lumbar cord segment (1000 µm radius and 3500 µm length). Given that NMDA and electrical intraspinal stimulation produce the same limited set of force directions (Saltiel et al. 1998), known for electrical stimulation not to depend on afferents (Giszter et al. 1993, Tresch and Bizzi 1999), NMDA effects unlikely represent afferent fiber stimulation. They likely represent postsynaptic effects on interneurons (Alpert and Alford 2013).

NMDA data analysis

Data recording and parsing, computing average force direction and EMGs during responses, and reconstructing EMGs with synergies

EMGs, amplified 25,000 times, and three-dimensional forces of the isometric hind limb were recorded at 2000 Hz for 60 s from the onset of NMDA iontophoresis. As previously described (Saltiel et al. 2005), we manually parsed the forces and EMGs, intersected the two, and determined the average force direction and EMGs during each response. The horizontal force direction notation is 0° rostral, ±180° caudal, 90° lateral, −90° medial (Fig. 1a inset). To correct for possible electrode sampling differences between frogs, we normalized each muscle EMG values to its maximal activity from any response in that frog. Using the seven synergies (A to G in Fig. 1b) previously extracted from the entire set of NMDA-elicited EMG responses, we used our non-negative least-squares factorization algorithm (Saltiel et al. 2001; Tresch et al. 1999) to find their activation coefficients as they reconstructed the EMGs. Figure 1 shows two examples (see "Results").

Identification of NMDA cycles of interest

We identified cycles consisting of a caudal extension (>165° or $\leq$ -142.5°)-lateral force (>0° and $\leq$165°)-flexion ($\leq$0° and $\geq$−45°) sequence. Because among two known types of caudal extensions (Saltiel et al. 2005), the type immediately preceding a lateral force within the same extension phase was the one based on synergy B in 80 % of cases (24/30), we focused on B synergy caudal extension-lateral force sequences. 18/24 of these sequences were followed by flexions, giving a full cycle. Since we previously found that flexions linked to B synergy caudal extensions begin without synergy C, we discarded 3/18 cycles where the flexion onset included synergy C. Thus, we studied 15 B synergy caudal extension-lateral force-flexion cycles.

Flexion onset was determined as previously (Saltiel et al. 2005), and considered not to include synergy C when F or E was most active, and had an arctangent with synergy $C \leq 22.5°$.

Determining the synergy sequence of the NMDA caudal extension-lateral force-flexion cycle

To focus on the synergies time course, we divided the caudal-lateral extension and flexion phases of each cycle into five equal intervals, and expressed each synergy ten response coefficients as a percentage of their cycle

maximum. In one method, boxes indicated for each synergy periods of activation above 70 %, with box height according to the relative order from most to least-activated synergies. The boxes' weighted centers were taken as the synergy activation times in each cycle. The second method used no threshold, but was simply an average across the caudal extension-lateral force-flexion cycles of the ten successive coefficients of synergies A to G.

Locomotion

Four intact frogs were implanted under anesthesia in the same muscles as the NMDA-studied spinal frogs, EMG wires led subcutaneously to a connector on the back, and signals amplified 5000x.

Locomotor EMG parsing and processing, and determining the locomotor synergy sequence

Because AM, SM, VI, VE are the key thigh muscles of caudal extension synergies B and D (Saltiel et al. 2005) and lateral force synergies G and D, and GA of ankle extensor synergy A, stance parsing was from first to last activity among these muscles. Swing was between stances, or if no step followed, till ST offset (last flexor). We analyzed 173 steps. Processing was as with NMDA, except that locomotor EMGs were not normalized. Flexors were more weakly activated than extensors across behaviors, and normalization would have inflated them artificially. However, we repeated an analysis (Fig. 7b) with non-normalized NMDA EMGs as in locomotion. Because we wish to compare the locomotor to the NMDA synergy sequence, and to the NMDA-derived synergy topography, we reconstructed the locomotor EMGs with the seven NMDA synergies. The locomotor synergy sequence was next determined using the same two methods as for NMDA.

Mapping synergies A to G

NMDA activated 110 sites in the ten frogs (at eight sites the limb was free, not isometric). Initial responses were from EMG onset on visual inspection, till the line joining the synergy composition of successive responses changed direction by $\geq 22.5°$. The initial response synergy coefficients were averaged and expressed to sum to 100 %, for equal contribution of each site.

When mapping individual sites, a site encoded synergy A when initial synergy A activation exceeded each of the other six synergies such that their arctangents with synergy A were all $\leq 30°$ (equivalent to a ratio ≥ 1.733). Because synergy A was a dominant synergy in the output (Fig. 6a), any synergy A amount was allowed when defining a

synergy B, C, D, E, F or G encoding site. Thus, a site encoded synergy B when initial synergy B activation exceeded each of synergies C to G such that their arctangents with synergy B were all $\leq 30°$.

We also divided the rostrocaudal cord in 10 bins. For same rostrocaudal location sites to be in the same bin, 10 bins of 11 sites were not possible. Among four possibilities of 8 bins of 11 sites, and 1 bin each of 12 and 10 sites, we chose the one where the distribution of bin dimensions gave the smallest mean square error from that of ten equally sized bins (1.2269 mm each). The synergies mean activations were plotted in each bin, at the mean location of its sites. For a broader perspective, we examined for each site, a second up to tenth set of responses (full series available at 85/110 sites) after the initial ones. For each bin, the percentages that synergies A to G contributed to the composition of each site second up to tenth set of responses were pooled and averaged. We did parametric and nonparametric statistical analyses on each synergy, to determine whether a rostrocaudal topography exists in the spinal cord (see "Appendix").

Comparison of spatial topography of synergies with synergy sequences of the step cycle

We computed the normalized dot product (ndp) between the 7-synergy vector of each of responses 1–10 of the step cycle, and the 7-synergy vector of each of the 10 bins of topography, and displayed the results in pseudocolor. This allowed to determine which rostrocaudal bin best matched each step response, and how this evolved over the course of the step. For this analysis, the locomotor and topography data were processed similarly, as explained in detail in "Results".

To assess if the rostrocaudal traveling wave specifically resulted from the topography, we did 10,000 random shuffles of the spinal cord sites locations, keeping each site 1st to 10th responses attached. We examined how often the Pearson correlations computed between the bin number best-matching the successive step responses (swing–stance cycle), and these step responses (renumbered from 1 to 10), were greater with the shuffled data than with the data.

For statistics on ndp between step responses and topographic bins, we processed the locomotion data slightly differently. Having again each step response seven synergy coefficients summing to 100 %, each synergy was normalized to a maximum of 100 % across each step cycle. Ndp were then computed between each individual step responses and each bin of the topography. Ndp of a given step response with two topographic bins could then be compared with t tests.

Simulations

We modeled a circuit to produce the locomotor synergy sequence A+B–G–A–F–E–G, using two layers as in the literature. The pattern formation (PF) layer has the synergy-encoding modules. We call the second layer, traveling wave (TW) layer, corresponding to the time-keeping rhythm generator in other models. However, a rostrocaudal activation will also occur in the PF layer.

The interneurons encoding synergies A, B, G, F, and E, with double representations of A and G as in the sequence, are represented by single neurons, firing according to Li model (2008):

$$\frac{dr_i}{dt} = -\frac{r_i}{\tau} + f\left(\sum_j W_{ij} r_j - T_i\right) + I_i$$

where r_i is the ith neuron firing rate, τ the time constant, W_{ij} the connection weight from neuron j to neuron i within the PF layer ($W_{ij}= 1$ or -1 when neuron j is excitatory or inhibitory), T_i the threshold, and I_i the external input from the TW to PF layer. The response function $f(.)$ is:

$$f(x) = \begin{cases} 0, & x \le 0, \\ \tanh(x), & x > 0. \end{cases}$$

When $I_i = 0$, neuron i will reach a steady maximal firing rate equal to τ, where $-r_i/\tau = -1$ cancels out the second term $f(.)$ (maximal value of tanh being equal to 1), such that $dr_i/dt = 0$.

When $T_i = 0$ for neuron i excited by neuron j, they will start firing at the same time, but neuron i will outlast neuron j, because $\tanh(r_j–T_i)$ will remain ≈ 1 as long as r_j remains above ~ 2 Hz. Thus, assuming $I_i = 0$, neuron i will continue firing at $r_i = \tau$, until r_j has declined to ~ 2 Hz, hence its delayed offset compared to neuron j. If instead T_i is high, neuron i onset will be delayed compared to neuron j, but the two neurons will start to turn off around the same time.

For the situation of a synergy both delayed in onset and offset compared to the previous one, we used two methods, inspired by delayed excitation mechanisms in the Tritonia swimming circuitry (Getting 1983). One method (neurons F and E in Fig. 9) used a time-varying threshold exponentially decreasing with time. This would resemble the delayed activation of a neuron until its A-current turned on by depolarization inactivates exponentially (Getting 1983; Connor and Stevens 1971). The other method used a dual excitatory/inhibitory input from neuron GG to A2, with slightly higher activation threshold of the inhibitory pathway, and appropriate threshold of A2. This may resemble the dual inhibitory–excitatory synapse described by Getting (1981, 1983).

A list of simulation parameters is provided in Table 4.

Appendix: statistical analyses on synergy rostrocaudal topography

We did both parametric and nonparametric statistical analyses on each synergy, to determine whether a rostrocaudal topography exists in the spinal cord.

The parametric analysis was a two-way mixed-design ANOVA, adapted for unequal ns (Ferguson and Takane 1989), with one independent factor (bin location, bins 1–10), and one repeated-measurements factor (the first up to tenth set of responses), i.e., 10×10 cells. The null hypothesis was no difference in synergy activation between the ten topographic bins. To achieve a better homogeneity of variance between the different bins, the data were square-root transformed prior to running the ANOVA (Ferguson and Takane 1989). Using F_{max}, the ratio of maximum to minimum variance across the 10 bins, computed separately for the 1st–10th responses and for each synergy, the square-root transformation greatly improved the homogeneity of variance, reducing the proportion of F_{max} greater than $F_{maxcrit}$ from 52/70 to 13/70 (Carter 2014). The ANOVA, when yielding a P value <.05 (6/7 synergies) was followed by post hoc contrast analyses, using Scheffé's method, comparing for each synergy a group of bins where it was most activated across the ten responses, to a group of bins where it was least activated. Because these are post hoc contrasts, the critical F value was appropriately multiplied by nine (number of bins minus one), and its first degree of freedom (contrast df) was also taken as 9 (Ferguson and Takane 1989; Howell 2007).

The nonparametric analysis on each synergy was a Mack–Skillings test which, like the Friedman test, is the nonparametric equivalent of a two-way ANOVA, but allows unequal ns (Hollander et al. 2014). The ten topographic bins and the 1st–10th responses were taken as treatments and blocks, respectively, and ranking from smallest to largest value was done separately within each block across the 110 sites in the 10 bins. Ranks were summed for each bin across the ten blocks, and the Mack–Skillings statistic computed (Mack and Skillings 1980, Eq. 2.4) to again test the null hypothesis of no difference in synergy activation between the ten topographic bins. For post hoc analyses, no complex contrast analysis seems available in the literature, and we, therefore, did post hoc multiple pairwise comparisons, using Mack–Skillings conservative Scheffé procedure for the proportional frequencies case (Mack and Skillings 1980, Eq. 4.1). The proportional frequency case ($n_{ij} = n_i \times n_j/N$, where n_{ij}, n_i, n_j, and N are the number of observations in cell of block i and treatment j, entire block i, entire treatment j, and all cells, respectively) seemed a legitimate approximation to our data because our actual n_{ij}s differed only slightly from

the expected proportional frequencies n_{ijs}. The absolute rounded differences were zero for 63 cells, one for 35 cells, and two for two cells. Moreover, the Mack–Skillings statistic changed only by 0.64 ± 0.30 % for the seven synergies when recomputed with the simplified proportional frequency formula (their Eq. 3.2).

As in the previous parametric analysis, the Scheffé method uses an experiment-wise error rate at the chosen alpha for the entire set of possible pairwise comparisons or other contrasts for a given synergy (Hollander et al. 2014), and no Bonferroni correction is necessary. Because Scheffé is very conservative, we accepted $P \leq .1$ as significant for the post hoc analyses (Ferguson and Takane 1989; Mack and Skillings 1980).

Compliance with ethical standards

Conflict of interest The authors declare that they have no conflict of interest.

References

Alpert MH, Alford S (2013) Synaptic NMDA receptor-dependent Ca^{2+} entry drives membrane potential and Ca^{2+} oscillations in spinal ventral horn neurons. PLoS One 8(4):e63154

Antri M, Mellen N, Cazalets JR (2011) Functional organization of locomotor interneurons in the ventral lumbar spinal cord of the newborn rat. PLoS One 6(6):e20529

AuYong N, Ollivier-Lanvin K, Lemay MA (2011) Preferred locomotor phase of activity of lumbar interneurons during air-stepping in subchronic spinal cats. J Neurophysiol 105:1011–1022

Berger DJ, Gentner R, Edmunds T, Pai DK, d'Avella A (2013) Differences in adaptation rates after virtual surgeries provide direct evidence for modularity. J Neurosci 33:12384–12394

Bizzi E, Cheung VC (2013) The neural origin of muscle synergies. Front Comput Neurosci 7:51. doi:10.3389/fncom.2013.00051

Bonnot A, Whelan PJ, Mentis GZ, O'Donovan MJ (2002) Spatiotemporal pattern of motoneuron activation in the rostral lumbar and the sacral segments during locomotor-like activity in the neonatal mouse spinal cord. J Neurosci 22(RC203):1–6

Burke RE, Degtyarenko AM, Simon ES (2001) Patterns of locomotor drive to motoneurons and last-order interneurons: clues to the structure of the CPG. J Neurophysiol 86:447–462

Butt SJ, Kiehn O (2003) Functional identification of interneurons responsible for left-right coordination of hindlimbs in mammals. Neuron 38:953–963

Carter A (2014) Critical values of F_{max} for Hartley's homogeneity of variance test. http://www.csulb.edu/~acarter3/course-biostats/tables/table-Fmax-values.pdf

Cazalets JR, Borde M, Clarac F (1995) Localization and organization of the central pattern generator for hindlimb locomotion in newborn rat. J Neurosci 15:4943–4951

Cazalets JR (2005) Metachronal propagation of motoneurone burst activation in isolated spinal cord of newborn rat. J Physiol 568(2):583–597

Chávez D, Rodriguez E, Jiménez I, Rudomin P (2012) Changes in correlation between spontaneous activity of dorsal horn neurons lead to differential recruitment of inhibitory pathways in the cat spinal cord. J Physiol 590:1563–1584

Cheng J, Jovanovic K, Aoyagi Y, Bennett DJ, Han Y, Stein RB (2002) Differential distribution of interneurons in the neural networks that control walking in the mudpuppy (Necturus maculatus) spinal cord. Exp Brain Res 145:190–198

Cheung VC, d'Avella A, Tresch MC, Bizzi E (2005) Central and sensory contributions to the activation and organization of muscle synergies during natural motor behaviors. J Neurosci 25:6419–6434

Cheung VC, Piron L, Agostini M, Silvoni S, Turolla A, Bizzi E (2009) Stability of muscle synergies for voluntary actions after cortical stroke in humans. Proc Natl Acad Sci 106:19563–19568

Churchland MM, Cunningham JP, Kaufman MT, Foster JD, Nuyujukian P, Ryu SI, Shenoy KV (2012) Neural population dynamics during reaching. Nature 487:51–56

Chvatal SA, Ting L (2012) Voluntary and reactive recruitment of locomotor muscle synergies during perturbed walking. J Neurosci 32:12237–12250

Cohen A (1988) Evolution of the central pattern generator for locomotion. In: Cohen AH, Rossignol S, Grillner S (eds) Neural control of rhythmic movements in vertebrates. John Wiley & Sons, New York, pp 129–166

Connor JA, Stevens CF (1971) Voltage clamp studies of a transient outward current in gastropod neural somata. J Physiol 213:21–30

Cowley KC, Zaporozhets E, Schmidt BJ (2010) Propriospinal transmission of the locomotor command signal in the neonatal rat. Ann N Y Acad Sci 1198:42–53

Cramer SW, Gao W, Chen G, Ebner TJ (2013) Reevaluation of the beam and radial hypotheses of parallel fiber action in the cerebellar cortex. J Neurosci 33:11412–11424

Cruce WL (1974) The anatomical organization of hindlimb motoneurons in the lumbar spinal cord of the frog, *Rana catesbiana*. J Comp Neurol 153:59–76

Cuellar CA, Tapia JA, Juárez V, Quevedo J, Linares P, Martínez L, Manjarrez E (2009) Propagation of sinusoidal electrical waves along the spinal cord during a fictive motor task. J Neurosci 29:798–810

d'Avella A, Portone A, Fernandez L, Lacquaniti F (2006) Control of fast-reaching movements by muscle synergy combinations. J Neurosci 26:7791–7810

Davis BL, Vaughan CL (1993) Phasic behavior of EMG signals during gait: use of multivariate statistics. J Electromyogr Kinesiol 3:51–60

Deliagina TG, Orlovsky GN, Pavlova GA (1983) The capacity for rhythmic oscillations is distributed in the lumbosacral spinal cord of the cat. Exp Brain Res 53:81–90

Dominici N, Ivanenko YP, Cappellini G, d'Avella A, Mondi V, Cicchese M, Fabiano A, Silei T, Di Paolo A, Giannini C, Poppele RE, Lacquaniti F (2011) Locomotor primitives in newborn babies and their development. Science 334:997–999

Dougherty KJ, Kiehn O (2010) Firing and cellular properties of V2a interneurons in the rodent spinal cord. J Neurosci 6:24–37

Ecker A (1971) The anatomy of the Frog (Haslam G, translator). Asher, Amsterdam

Falgairolle M, Cazalets JR (2007) Metachronal coupling between spinal neuronal networks during locomotor activity in newborn rat. J Physiol 580:87–102

Ferguson GA, Takane Y (1989) Statistical analysis in psychology and education, 6th edn. McGraw-Hill, New York, chapters 15, 16, 18 and 19

Freeman JA, Nicholson CN (1970) Space-time transformation in the frog cerebellum through an intrinsic tapped delay-line. Nature 226:640–642

Getting PA (1981) Mechanisms of pattern generation underlying swimming in *Tritonia* I. Network formed by monosynaptic connections. J Neurophysiol 46:65–79

Getting PA (1983) Mechanisms of pattern generation underlying swimming in *Tritonia* III. Intrinsic and synaptic mechanisms for delayed excitation. J Neurophysiol 49:1036–1050

Giszter SF, Mussa-Ivaldi FA, Bizzi E (1993) Convergent force fields organized in the frog's spinal cord. J Neurosci 13:467–491

Grillner S (1981) Control of locomotion in bipeds, tetrapods, and fish. In: Brooks VB (ed) Handbook of physiology. The nervous system. Motor control, vol. 2. Bethesda, Maryland, pp 1179–1236

Hägglund M, Dougherty KJ, Borgius L, Itohara S, Iwasato T, Kiehn O (2013) Optogenetic dissection reveals multiple rhythmogenic modules underlying locomotion. Proc Natl Acad Sci 110:11589–11594

Hart CB, Giszter SF (2010) A neural basis for motor primitives in the spinal cord. J Neurosci 30:1322–1336

Hinckley CA, Pfaff SL (2013) Imaging spinal neuronal ensembles active during locomotion with genetically encoded calcium indicators. Ann N Y Acad Sci 1279:71–79

Hollander M, Wolfe DA, Chicken E (2014) Nonparametric statistical methods, sect. 7.9–7.10, 3rd edn. Wiley, Hoboken, pp 354–369

Howell DC (2007) Statistical methods for psychology. 7th edn. Wadsworth, Cengage Learning, Belmont, chapter 12

Hulshof JB, de Boer-van Huizen R, ten Donkelaar HJ (1987) The distribution of motoneurons supplying hindlimb muscles in the clawed toad Xenopus laevis. Acta Morphol Neerl Scand 25:1–16

Ivanenko YP, Poppele RE, Lacquaniti F (2004) Five basic muscle activation patterns account for muscle activity during human locomotion. J Physiol 556(1):267–282

Ivanenko YP, Poppele RE, Lacquaniti F (2006a) Spinal cord maps of spatiotemporal alpha-motoneuron activation in humans walking at different speeds. J Neurophysiol 95:602–618

Ivanenko YP, Poppele RE, Lacquaniti F (2006b) Motor control programs and walking. Neuroscientist 12:339–348

Jankowska E (2008) Spinal interneuronal networks in the cat: elementary components. Brain Res Rev 57:46–55

Kjaerulff O, Kiehn O (1996) Distribution of networks generating and coordinating locomotor activity in the neonatal rat spinal cord in vitro: a lesion study. J Neurosci 75:1472–1482

Klein Breteler MD, Simura K, Flanders M (2007) Timing of muscle activation in a hand movement sequence. Cereb Cortex 17:803–815

Krouchev N, Drew T (2013) Motor cortical regulation of sparse synergies provides a framework for the flexible control of precision walking. Front Comput Neurosci 7:83. doi:10.3389/fncom.2013.00083

Krouchev N, Kalaska JF, Drew T (2006) Sequential activation of muscle synergies during locomotion in the intact cat as revealed by cluster analysis and direct decomposition. J Neurophysiol 96:1991–2010

Kwan AC, Dietz SB, Zhong G, Harris-Warrick RM, Webb WW (2010) Spatiotemporal dynamics of rhythmic spinal interneurons measured with two-photon calcium imaging and coherence analysis. J Neurophysiol 104:3323–3333

Lennard PR (1985) Afferent perturbations during "monopodal" swimming movements in the turtle: phase-dependent cutaneous modulation and proprioceptive resetting of the locomotor rhythm. J Neurosci 5:1434–1445

Levine AJ, Lewallen KA, Pfaff SL (2012) Spatial organization of cortical and spinal neurons controlling motor behaviour. Curr Opin Neurobiol 22:812–821

Levine AJ, Hinckley CA, Hilde KL, Driscoll SP, Poon TH, Montgomery JM, Pfaff SL (2014) Identification of a cellular node for motor control pathways. Nat Neurosci 17:586–593

Li C (2008) Functions of neuronal network motifs. Phys Rev E 78:037101

Loeb EP, Giszter SF, Saltiel P, Mussa-Ivaldi FA, Bizzi E (2000) Output units of motor behavior: an experimental and modeling study. J Cognit Neurosci 12:78–97

Lomeli J, Quevedo J, Linares P, Rudomin P (1998) Local control of information flow in segmental and ascending collaterals of single afferents. Nature 395:600–604

Mack GA, Skillings JH (1980) A Friedman-type rank test for main effects in two-factor ANOVA. J Am Statist Assoc 75:947–951

Manjarrez E, Jiménez I, Rudomin P (2003) Intersegmental synchronization of spontaneous activity of dorsal horn neurons in the cat spinal cord. Exp Brain Res 148:401–413

Marcoux J, Rossignol S (2000) Initiating or blocking locomotion in spinal cats by applying noradrenergic drugs to restricted lumbar spinal segments. J Neurosci 20:8577–8585

Markin SN, Lemay MA, Prilutsky BI, Rybak IA (2012) Motoneuronal and muscle synergies involved in cat hindlimb control during fictive and real locomotion: a comparison study. J Neurophysiol 107:2057–2071

McCrea DA, Rybak IA (2008) Organization of mammalian locomotor rhythm and pattern generation. Brain Res Rev 57:134–146

O'Donovan MJ, Bonnot A, Mentis GZ, Arai Y, Chub N, Schreider NA, Wenner P (2008) Imaging the spatiotemporal organization of neural activity in the developing spinal cord. Develop Neurobiol 68:788–803

Olree KS, Vaughan CL (1995) Fundamental patterns of bilateral muscle activity in human locomotion. Biol Cybern 73:409–414

Overduin SA, d'Avella A, Carmena JM, Bizzi E (2012) Microstimulation activates a handful of muscle synergies. Neuron 76:1071–1077

Patla AE (1985) Some characteristics of EMG patterns during locomotion: implications for the locomotor control process. J Motor Behav 17:443–461

Pérez T, Tapia JA, Mirasso CR, Garcia-Ojalvo J, Quevedo J, Cuellar CA, Manjarrez E (2009) An intersegmental neuronal architecture for spinal wave propagation under deletions. J Neurosci 29:10254–10263

Puskàr Z, Antal M (1997) Localization of last-order premotor interneurons in the lumbar spinal cord of rats. J Comp Neurol 389:377–389

Rivest F, Kalaska JF, Bengio Y (2010) Alternative time representation in dopamine models. J Comput Neurosci 28:107–130

Roh J, Cheung VC, Bizzi E (2011) Modules in the brainstem and spinal cord underlying motor behaviors. J Neurophysiol 106:1363–1378

Rudomin P (2002) Selectivity of the central control of sensory information in the mammalian spinal cord. Adv Exp Med Biol 508:157–170

Rybak IA, Shevtsova NA, Lafreniere-Roula M, McCrea DA (2006) Modelling spinal circuitry involved in locomotor pattern generation: insights from deletions during fictive locomotion. J Physiol 577:617–639

Saltiel P, Rossignol S (2004a) Critical points in the forelimb fictive locomotor cycle and motor coordination: evidence from the effects of tonic proprioceptive perturbations in the cat. J Neurophysiol 92:1329–1341

Saltiel P, Rossignol S (2004b) Critical points in the forelimb fictive locomotor cycle and motor coordination: effects of phasic retractions and protractions of the shoulder in the cat. J Neurophysiol 92:1342–1356

Saltiel P, Tresch MC, Bizzi E (1998) Spinal cord modular organization and rhythm generation: an NMDA iontophoretic study in the frog. J Neurophysiol 80:2323–2339

Saltiel P, Wyler-Duda K, d'Avella A, Tresch MC, Bizzi E (2001) Muscle synergies encoded within the spinal cord: evidence from focal intraspinal NMDA iontophoresis in the frog. J Neurophysiol 85:605–619

Saltiel P, Wyler-Duda K, d'Avella A, Ajemian R, Bizzi E (2005) Localization and connectivity in spinal interneuronal networks: the adduction–caudal extension–flexion rhythm in the frog. J Neurophysiol 94:2120–2138

Schneider SP (1992) Functional properties and axon terminations of interneurons in laminae III–IV of the mammalian spinal dorsal horn in vitro. J Neurophysiol 68:1746–1759

Schneider SP (2003) Spike frequency adaptation and signalling properties of identified neurons in rodent deep spinal dorsal horn. J Neurophysiol 90:245–258

Stein PSG (2008) Motor pattern deletions and modular organization of turtle spinal cord. Brain Res Rev 57:118–124

Székely G, Czéh G (1971) Muscle activities of partially innervated limbs during locomotion in Ambystoma. Acta Physiol Acad Sci Hung 40:269–286

Ting LH, Macpherson JM (2004) A limited set of muscle synergies for force control during a postural task. J Neurophysiol 93:609–613

Tresch MC, Kiehn O (1999) Coding of locomotor phase in populations of neurons in rostral and caudal segments of the neonatal rat lumbar spinal cord. J Neurophysiol 82:3563–3574

Tresch MC, Saltiel P, Bizzi E (1999) The construction of movement by the spinal cord. Nature Neurosci 2:162–167

Tripodi M, Stepien AE, Arber S (2011) Motor antagonism exposed by spatial segregation and timing of neurogenesis. Nature 479:61–66

Yakovenko S, Mushahwar V, VanderHorst V, Holstege G, Prochazka A (2002) Spatiotemporal activation of lumbosacral motoneurons in the locomotor step cycle. J Neurophysiol 87:1542–1553

Yakovenko S, Krouchev N, Drew T (2011) Sequential activation of motor cortical neurons contributes to intralimb coordination during reaching in the cat by modulating muscle synergies. J Neurophysiol 105:388–409

Zhong G, Droho S, Crone SA, Dietz S, Kwan AC, Webb WW, Sharma K, Harris-Warrick RM (2010) Electrophysiological characterization of V2a interneurons and their locomotor-related activity in the neonatal mouse spinal cord. J Neurosci 30:170–182

Zhong G, Shevtsova NA, Rybak IA, Harris-Warrick RM (2012) Neuronal activity in the isolated mouse spinal cord during spontaneous deletions in fictive locomotion: insights in locomotor central pattern generator organization. J Physiol 590(19):4735–4759

Zipser D (1986) A model of hippocampal learning during classical conditioning. Behav Neurosci 100:764–776